The MAVEN Magnetic Field Investigation

J. E. P. Connerney, J. Espley, P. Lawton, S. Murphy,
J. Odom, R. Oliversen, and D. Sheppard

NASA Goddard Space Flight Center
Solar System Exploration Division
Planetary Magnetospheres Laboratory
Greenbelt, MD 20771

November 1, 2014

Corresponding author: J. Connerney
Email: jack.connerney@nasa.gov
Phone: 301-286-5884
Fax no: 301-286-3346

Abstract: The MAVEN magnetic field investigation is part of a comprehensive particles and fields subsystem that will measure the magnetic and electric fields and plasma environment of Mars and its interaction with the solar wind. The magnetic field instrumentation consists of two independent tri-axial fluxgate magnetometer sensors, remotely mounted at the outer extremity of the two solar arrays on small extensions ("boomlets"). The sensors are controlled by independent and functionally identical electronics assemblies that are integrated within the particles and fields subsystem and draw their power from redundant power supplies within that system. Each magnetometer measures the ambient vector magnetic field over a wide dynamic range (to 65,536 nT per axis) with a quantization uncertainty of 0.008 nT in the most sensitive dynamic range and an accuracy of better than 0.05%. Both magnetometers sample the ambient magnetic field at an intrinsic sample rate of 32 vector samples per second. Telemetry is transferred from each magnetometer to the particles and fields package once per second and subsequently passed to the spacecraft after some reformatting. The magnetic field data volume may be reduced by averaging and decimation, when necessary to meet telemetry allocations, and application of data compression, utilizing a lossless 8-bit differencing scheme. The MAVEN magnetic field experiment may be reconfigured in flight to meet unanticipated needs and is fully hardware redundant. A spacecraft magnetic control program was implemented to provide a magnetically clean environment for the magnetic sensors and the MAVEN mission plan provides for occasional spacecraft maneuvers – multiple rotations about the spacecraft x and z axes – to characterize spacecraft fields and/or instrument offsets in flight.

I) Introduction

The Mars Atmosphere and Volatile EvolutioN (MAVEN) mission seeks to understand the history of climate change on Mars by studying the present state of the Mars upper atmosphere and ionosphere, and the processes governing atmospheric loss to space [*Jakosky et al.,* 2014]. Mars has a thin and dusty atmosphere comprised primarily of carbon dioxide (96%), argon (~2%) and nitrogen (~2%) with traces of carbon monoxide, water, oxygen, and other gases. The temperatures and pressures in the Mars lower atmosphere are comparable to those found in the Earth's stratosphere. With a surface pressure of only about 1% of Earth's, and temperatures well below 273 K, it is difficult to reconcile the thin atmosphere we see today with the geological evidence (channels, valley networks, erosional features, small scale layering, and aqueous mineralogy) that suggest water flowed on Mars until about 4 billion years ago.

The preponderance of geologic evidence suggests that early Mars had a warm and dense atmosphere and perhaps an ocean, if not standing water, persisting for a geologically significant period. If so, where is this water today, and what became of the dense atmosphere? Mars is not so massive as to trap volatile species indefinitely, so while loss processes remain poorly understood, atmospheric loss to space is a prime candidate for their removal. Indeed, ample evidence of an enrichment of heavy isotopes ($^{15}N/^{14}N$, $^{38}Ar/^{36}Ar$, and D/H) in the atmosphere [*Jakosky and Phillips*, 2001; *Mahaffy et al.,* 2013] and direct measurements of escaping ions made by orbiting spacecraft [*Barabash et al.*, 2007; *Nilsson et al.*, 2011] implicate loss to space as a significant, if not dominant, loss mechanism throughout Mars history.

The Mars atmosphere no longer enjoys the protection from the solar wind afforded by the presence of a global magnetic field of appreciable magnitude. However, early Mars did have an Earth-like magnetic field of sufficient strength to shelter the atmosphere from the solar wind [*Acuña et al.*, 1998; 1999; 2001]. So it is tempting to speculate that a warm and dense Mars atmosphere existed within the protection afforded by an early Mars dynamo, and the demise of the dynamo, some 4 billion years ago, exposed the atmosphere to stripping by the solar wind. Had Mars retained a dynamo, would it be more habitable today? To answer this question we need understand the processes at work in the Mars atmosphere, and how to use that knowledge to infer the evolutionary

history of the atmosphere. There is also evidence for sequestration of water and possibly other volatiles in the Mars regolith, especially at mid and high latitudes.

The MAVEN spacecraft will spend more than a Mars year in polar orbit, sampling the Mars space environment with a full suite of in-situ and remote sensing instruments [*Jakosky et al*., 2014]. These instruments are designed to provide the measurements necessary to characterize the upper atmosphere and ionosphere; quantify the current rate of escape of atmospheric constituents under a variety of solar wind conditions; and by backward extrapolation (more accurately, modeling) quantify the total atmospheric loss to space throughout Mars history. In looking back through time, we must bear in mind that our young Sun was likely far more active than at present, characterized by dramatically more violent outflows than we see today. The MAVEN prime mission is designed to observe the solar wind interaction with Mars during the declining phase of the current solar cycle, which thus far appears unremarkable but for a relatively weak sunspot activity.

II) Science Objectives

a. Mars Magnetic Field

The discovery of the intense magnetization of the Mars crust is one of the most remarkable findings of the exploration of Mars, and one of the most illuminating. The Mars Global Surveyor (MGS) mission established that Mars has no global magnetic field, and therefore no dynamo at present, but it must have had one in the past when the crust acquired intense remanent magnetization. It is likely that a molten iron core formed early, after or during hot accretion 4.5-4.6 Ga, and for at least a few hundred million years a substantial global field was generated by dynamo action in the core. The chronology proposed by *Acuña et al*. [1999] attributes the global distribution of magnetization to the early demise of the dynamo, prior to the last great impacts (~4 Ga) that left large unmagnetized basins in the crust. This view has been supported by more complete analyses of the large impact basins [*Lillis et al.*, 2008; *Lillis et al.*, 2013], leading to more precise estimates of the dynamo's demise. It appears that dynamo generation of the global magnetic field was extinguished before formation of Hellas and Utopia basins approximately 4.0-4.1 Ga.

Early onset and cessation of the dynamo is difficult to reconcile with the notion of a dynamo driven by solidification of an inner core [*Schubert et al.,* 1992], the preferred energy source for the Earth's dynamo. Alternatively, an early dynamo can be driven by thermal convection, with or without plate tectonics, for the first 0.5 – 1 Gyr [*Breuer and Spohn*, 2003; *Schubert and Spohn*, 1990; *Stevenson et al.,* 1983; *Connerney et al*., 2004], persisting as long as the core heat flow remains above a critical threshold for thermal convection [*Nimmo and Stevenson*, 2000]. With knowledge that Mars had a substantial global magnetic field billions of years ago, it is quite natural to consider whether the Mars atmosphere may have been sheltered from the solar wind for a geologically significant period. In the dynamo era, Mars may have retained a warm and dense atmosphere, only to lose it subsequent to decay of the global field. Did the Mars dynamo prevent loss of atmosphere to space?

There is also a supply side argument to be made on behalf of the Mars dynamo, if only indirectly. The supply side argument follows from interpretation of the crustal magnetic imprint within the framework of plate tectonics. A planetary dynamo is driven by vigorous convective motions in the core, resulting from a temperature gradient across the core-mantle boundary. The thermal gradient persists as long as an efficient cooling mechanism (e.g., mantle convection, and plate tectonics) is maintained. Following this line of thought, the demise of the dynamo may be associated with cessation of plate tectonics. On earth, we associate plate tectonics with active geological processes: crustal subduction, mantle convection, active volcanism, and consequently venting of gases from the interior. This is the rationale for a supply side argument: maintenance of a dense atmosphere via the active geologic processes associated with mantle convection, subduction, and volcanism.

After more than 2 full Mars years of mapping operations, MGS produced an unprecedented global map of magnetic fields produced by remanent magnetism in the crust. This map (**Figure 1**) reveals contrasts in magnetization that appear in association with known faults; variations in magnetization clearly associated with volcanic provinces; and magnetic field patterns reminiscent of transform faults at spreading centers [*Connerney et al,* 2005]. *Connerney et al.* proposed that the entire crust acquired a magnetic imprint via crustal spreading and cooling in the presence of a reversing dynamo; and that erasure of this imprint occurred where the crust was buried (thermal demagnetization) by flood basalts to depths of a few km. Transform faults are unique to plate tectonics, so if these features are indeed

transform faults then the Mars crust formed via sea floor spreading as on Earth [*Connerney et al.,* 1999; *Sleep,* 1990].

The magnetic record is complemented by geomorphological analyses that are suggestive of plate tectonics having occurred on Mars early in its history. The alignment of the great volcanic edifices on Mars is consistent with plate motion over a mantle plume [*Connerney et al.*, 2005] or, conversely, volcanic chains formed above subducting slabs [*Sleep,* 1990 ; *Sleep,* 1994; *Yin, personal communication*, 2012]. The topographical relief along much of the dichotomy boundary has been interpreted as a series of ridge/transform fault segments [*Sleep*, 1994]. A recent structural analysis of the Valles Marineris fault zone [*Yin,* 2012] likens this trough system to the left-slip, transtensional Dead Sea fault zone on Earth: an undisputed plate boundary. It is difficult to understand how such a structure evolved on Mars in the absence of plate tectonics.

Is it possible that a warm and dense atmosphere on Mars was supplied by outgassing associated with plate tectonics? If so, the Mars dynamo may have been instrumental in both the supply and maintenance of an early dense atmosphere. The fate of Mars' atmosphere may well be inseparable from cessation of plate tectonics and the demise of the dynamo; a marker for the evolution of Mars as a planet.

b. Interaction with the Solar Wind

Mars stands as an obstacle to the *solar wind*, the high velocity (supersonic) stream of plasma emanating from the sun. The expanding solar wind drags the frozen-in *interplanetary magnetic field* (IMF) along with it, and forms a multi-tiered interaction region about Mars as it interacts with the extended atmosphere and electrically-conducting conducting ionosphere (**Figure 2**). The characteristics of the solar wind interaction with a weakly magnetized, or unmagnetized body are in some regards similar to the flow about a magnetized planet [*Luhmann et al,* 1992; *Brain*, 2006], but for the lack of a global-scale *magnetosphere* within which the motion of charged particles is governed by an intrinsic planetary magnetic field.

Since the solar wind is supersonic, a *bow shock* forms upstream of Mars (**Figure 2**). The slowed, shocked solar wind flows around the obstacle within the *magnetosheath*, a turbulent region [*Espley et al.*, 2004] bounded by the bow shock and a lower boundary, often referred to as the *magnetic pile-up*

boundary [*Bertucci et al.,* 2003], or alternatively the *induced magnetosphere boundary* [e.g., *Brain et al*., 2015] or *induced magnetopause*. It marks the narrow transition between plasma dominated by ions of solar wind origin and plasma dominated by ions of planetary origin; it is often approximated by a paraboloid of revolution about the planet-sun line. The magnetic field extends well downstream in the anti-sunward direction, in effect draped around the conducting obstacle, to form the *magnetotail*, by analogy with the magnetotail that forms downstream of a magnetic planet. A magnetic planet imposes a geometry and polarity on the field in its magnetotail, whereas the magnetotail formed downstream of an unmagnetized body changes direction in response to changes in the direction of the interplanetary magnetic field.

However, Mars is neither an unmagnetized body, such as Venus, nor a magnetized body, like Earth. Where the Mars crust is intensely magnetized it can establish order over scale lengths of hundreds of kilometers much in the way the Earth's field does. In the Earth's upper atmosphere and ionosphere, a complex system of currents flow in response to solar heating of the atmosphere, particularly where horizontal magnetic fields are encountered (equatorial fountain effect and electrojet), and in response to the imposition of electric potentials (in particular, auroral ovals). By analogy to magnetized planets, field-aligned currents, called *Birkeland currents*, flow along the magnetic field and deposit energy into the electrically conducting ionosphere, particularly during solar storms, leading to auroral displays. Auroral emissions have been observed on Mars [*Bertaux et al.,* 2005; *Brain et al.,* 2006; *Lundin et al.,* 2006; *Brain and Halekas*, 2012.] in association with the most intensely magnetized regions of the southern highlands. On earth, and other planets with (dipolar) magnetic fields, auroral displays are most often observed in the polar regions. In contrast, on Mars, auroral emissions are observed in association with intense crustal magnetic fields that are strong enough to sustain magnetic fields to great heights, well above the ionosphere. **Figure 3** illustrates the complexity of the magnetic field observed in a meridian plane projection over the southern highlands, extending throughout the Mars upper atmosphere and ionosphere. The MAVEN spacecraft will sample the magnetic field and plasma environment throughout this region from about 120 km upwards, during "deep dip" campaigns and nominal orbital operations.

The crustal fields are strong enough to dramatically alter the nature of the interaction with the solar wind, as can be seen in the multi-fluid magnetohydrodynamic simulation [*Dong et al., 2014*] illustrated

in **Figure 4**. Field magnitudes are appreciably larger in regions of strong crustal fields than they would otherwise be, creating "mini-magnetospheres" where charged particle motion is guided by persistent, and stable, magnetic geometries. The geometry imposed by strong crustal fields dictates where field lines threading the ionosphere link with the solar wind and distant plasma environments, giving rise to deposition of energy and aurorae. The strong crustal fields can also impose a polarity and geometry in the magnetotail as they are drawn tailward by the solar wind [*Brain et al*., 2010]. Numerical simulations have amply demonstrated that the strong magnetic fields associated with the southern highlands have a shielding effect that reduces the ion escape flux [*Ma et al*, 2004; *Dong et al.*, 2014].

In collisionless plasmas, waves provide one of the main ways of distributing energy across the system. Ion cyclotron waves are produced when ions move in resonance with the magnetic fields. This produces fluctuations in the magnetic field with frequencies that depend on the mass and charge state of the ions producing them. Additionally, the highly turbulent Martian magnetosheath offers an unusual plasma environment where nonlinear (i.e. $\delta B \sim |B|$) kinetic plasma modes develop [*Glassmeier and Espley*, 2006]. Some groups have examined the role that plasma wave heating may play in the escape of atmosphere [*Ergun et al.,* 2006; *Andersson et al.,* 2010] but this task will be easier once the full Poynting flux is available using data from both the MAVEN MAG and LPW instruments.

Magnetic reconnection is another important plasma process that may play an important role in bulk atmospheric escape [*Brain et al.,* 2010]. Magnetic reconnection may occur when anti-parallel (or nearly so) magnetic fields are brought together in a plasma, resulting in a localized exception to the frozen-in condition of the magnetic field. This allows magnetic fields to reconfigure ("reconnect") and in the process magnetic energy is converted into thermal energy. Energization of the plasma can enhance atmospheric escape but the geometrical consequences of reconnection could be at least as important. The reconfiguration of the magnetic field may allow field lines that were connected to the IMF to lose that connection; conversely, reconfiguration may at times facilitate continuity with the IMF. *Halekas et al.* [2009] found many observations indicative of reconnection at Mars, suggesting that reconnection may not be uncommon. The first of its kind, fully instrumented particles and fields package (PFP) onboard MAVEN will allow careful investigation of this possibility.

The measurement of magnetic fields at Mars is therefore important to a variety of interrelated scientific topics, all bearing on the processes that control atmospheric loss to space. Characterizing the magnetic fields throughout the interaction region provides an interpretative framework to help us understand the complicated hybrid induced-crustal magnetosphere. In addition, the magnetic field magnitude and geometry are critical for understanding the trajectories of potentially escaping charged particles. The MAVEN Magnetic Fields Investigation plays an important role in understanding the role of plasma waves, reconnection, and bulk plasma structures in facilitating atmospheric escape and more broadly in the dynamics of the solar wind interaction.

III) Science Requirements

The magnetometer investigation (MAG) driving requirements benefit from a detailed knowledge of the magnetic field environment that MAVEN will transit, a consequence of the Mars Global Surveyor magnetic mapping. The MAVEN MAG requirements are sourced from the MAVEN Mission Requirements Document (MAVEN-PM-RQMT-0005), the MAVEN Level 3 Functional Requirements – Particle & Fields Functional Requirements Document (MAVEN-PFIS-RQMT-0016), and the MAVEN Magnetometer Level 4 Functional Requirements Document (MAVEN-MAG-RQMT-0061). The instrument requirements as follows:

- Measure the magnitude and direction of the ambient magnetic field;
- Provide the vector magnetic field (broadcast vector) to other science payloads in flight;
- Encompass a dynamic range of measurement from 3 nT to 3000 nT;
- Measurement accuracy & resolution of 1% or better;
- Sample rate providing temporal resolution of 20 seconds or better;
- Provide complete hardware redundancy of magnetic field measurement;
- Sensor orthogonality and alignment knowledge to 0.25 degrees or better;
- Provide non-magnetic a/c heaters for sensor thermal control, operating and non-operating.

Magnetometer Sensor Performance	
Sensor type	Dual tri-axial ring core fluxgates
Accuracy	0.05% absolute vector accuracy
Intrinsic noise level	0.015 nT (most sensitive range)
Attitude knowledge	Better than 0.05 degrees
Zero level stability	< 1 nT
Dynamic ranges (resolution)	512 nT (± 0.015 NT) 2048 nT (± 0.062 nT) 65536 nT (± 2.0 nT)
Intrinsic sample rate	32 vector samples/second
Radiation total ionizing dose (TID)	> 50 krad (at component level)

A more complete study of the magnetic field magnitudes that MAVEN may sample, between target altitudes of 125 and 400 km, was performed to optimize the choice of instrument dynamic ranges. Since MAVEN's mission plan does not target specific latitudes/longitudes, we need be prepared for the maximum field magnitude that might be experienced above the surface of the planet at altitudes in excess of ~100 km. This study demonstrated that it is very unlikely that a dynamic range of 512 nT might be exceeded throughout the entire mission, including the "deep dip" orbits. The magnetometer system provided as part of the Particles and Fields Package meets and exceeds the Project requirements with a pair of independent magnetic sensors with the following performance characteristics:

IV) Investigation Design and Spacecraft Accommodation

a. Investigation Design

The MAVEN particles and fields instrumentation form an ensemble of instruments ("Particles and Fields Package") controlled by a single hardware-redundant data processing unit (PFDPU) interfacing to the spacecraft. The PFP (**Figure 5**) services the Solar Wind Electron Analyzer (SWEA) instrument [*Mitchell et al.,* 2014], the Solar Wind Ion Analyzer (SWIA) instrument [*Halekas et al*., 2014], the Langmuir Probe and Waves (LPW) instrument [*Andersson et al.,* 2014], the Extreme Ultraviolet (EUV) instrument, the Solar Energetic Particles (SEP) instrument, and the (STATIC) instrument [*McFadden et al.,* 2014] in addition to the Magnetometer instrumentation (MAG). The MAVEN magnetic field investigation (MAG) consists of two independent and identical fluxgate magnetometer systems that are interfaced to and controlled by the PFDPU. The particles and fields electronics package is a stack of individual electronics boxes (**Figure 6**) that service each of the instruments; two of the "slices" are occupied by identical magnetometer electronics frames that service the two magnetometer sensors. Each electronics box is fully shielded and each draws power from the redundant power supplies within the PFP.

Individual and independent a/c heater electronics assemblies provide thermal control for the MAG sensors and are also accommodated on separate cards elsewhere within the PFP. These are powered directly by the spacecraft, providing uninterruptable power for sensor thermal control regardless of the state (on or off) of the PFP. The a/c heaters are proportional controllers that maintain sensor temperature within comfortable operational limits. They are designed to insure that no dc currents can circulate in the resistive heater elements that are placed underneath the sensor base and within the sensor thermal blanketing. (The spacecraft heaters are direct current powered and are therefore not suitable for use in proximity with a magnetic sensor).

The magnetometer sensors are located at the very end of the solar array panels on modest extensions (.66 m in length) designated as MAG "boomlets", placing them approximately 5.6 m from the center of the spacecraft body (**Figure 7**). Magnetometer sensors are best accommodated remotely, as far from spacecraft subsystems as is practical, to minimize the relative contribution of spacecraft-generated magnetic fields. Care is taken to minimize the magnetic signature of spacecraft

subsystems, of course, but one of the most effective ways to reduce spacecraft-generated magnetic fields is to separate spacecraft systems and sensor, taking maximum advantage of the $1/r^3$ diminution of a magnetic (dipole) source with distance from the source. Thus magnetometer sensors are often accommodated on a lengthy dedicated magnetometer boom that is deployed after launch. Alternatively, they may be accommodated at the outer extremity of the solar arrays, taking advantage of an essential appendage that also deploys post-launch. MAVEN took the latter approach, much as its predecessor Mars Global Surveyor did [*Acuña et al.*, 2001].

In typical implementations, a pair of magnetic sensors ("dual magnetometer technique") provides hardware redundancy as well as a capability to detect magnetic fields at two locations on the spacecraft. This capability offers the potential to monitor spacecraft generated magnetic fields in flight, by comparison of the field measured by each sensor. When both sensors are mounted along a radius vector on a dedicated magnetometer boom, one "outboard" and one "inboard", one can take advantage of the $1/r^3$ diminution of the (dipolar) field of the spacecraft with distance along the boom to identify local sources and separate the fields due to local sources from the ambient field. The outboard sensor is typically allocated the majority of the spacecraft telemetry allocation for the investigation, and sampled at a higher rate than the inboard sensor, anticipating a spacecraft field that changes slowly in time (this is not always the case!). Thus the outboard sensor is the primary sensor, and the inboard sensor is the secondary sensor, though in many implementations their role may be reversed if desired.

The MAVEN magnetometer sensors are located on the +Y spacecraft solar array ("outboard") and the –Y spacecraft solar array ("inboard"). The assignment is arbitrary, and in keeping with prior missions (Mars Observer, Mars Global Surveyor) and software heritage; you may prefer to think of the +Y sensor as the primary sensor, and –Y as the secondary sensor. In reality, they are identical, and each sensor is capable of performing either role. It was anticipated that the +Y sensor ("outboard" or primary sensor) location would be preferred over the –Y sensor location, from a spacecraft magnetic interference perspective, by virtue of the location of various components on the body of the spacecraft (reaction wheels in particular). Thus the +Y sensor was designated as primary sensor ("outboard"), and –Y sensor as secondary sensor; observations of the magnetic field during cruise operations confirmed this expectation. In early cruise, the inboard or secondary

sensor was sampled at a lesser rate, but as of June 2014, our current practice is to utilize the same sample rate for both sensors for diagnostic purposes.

b. Spacecraft Requirements

Instrument accommodation is always of concern for a magnetometer investigation, extending beyond the mechanical and thermal interfaces discussed above. Since the magnetometer sensors measure the ambient magnetic field, any appreciable spacecraft-generated magnetic fields may interfere with accurate measurement of the environmental field. The magnetic field produced by the spacecraft is managed via a spacecraft magnetic control plan that tracks the expected magnetic field at the sensor locations, and manages the net field at the sensors to meet a requirement appropriate to the mission. In recognition of the relatively weak field of the solar wind at Mars, the Project adopted a spacecraft magnetic field requirement not to exceed (NTE) 2 nT static and 0.25 nT variable. The static field is allocated a larger limit because with periodic spacecraft maneuvers a static magnetic field may be measured and corrected analytically.

c. Spacecraft Magnetic Control Plan

During the spacecraft design phase, and through assembly, test, and launch operations (ATLO), a magnetic model of the spacecraft was maintained as part of the spacecraft magnetic control program. This model accounts for the location and magnetic moment of spacecraft components and subsystems, and provides an estimate of the resultant spacecraft magnetic field, summed vectorially over its many parts, at the magnetometer sensor locations. The model is used to help allocate a fraction of the total NTE requirement to various subsystems and to guide mitigation where necessary. For example, when preliminary magnetic testing of the reaction wheel assemblies (RWA) indicated that they would contribute excessively to the variable (ac) spacecraft field, the Project responded with magnetic shielding enclosures for the RWAs that lessened their contribution by about an order of magnitude.

Spacecraft components, subsystems, and instruments were characterized by magnetic test at the Lockheed Martin Waterton Canyon facility or at subcontractor facilities. Test articles included engineering models that were available early in the program and for some subsystems and instruments, flight or qualification models. The solar arrays were carefully designed with compensation loops to null the magnetic signature of the array under illumination. This was accomplished by compensating each individual cell string with a matched compensation loop on the underside of the panel ("backwiring"). Verification testing of the solar array compensation scheme was performed on a qualification panel tested at LM's Sunnyvale facility. This test consists of exciting the compensated string with a square-wave current and measurement of the resultant magnetic field with a magnetic gradiometer, using synchronous detection to accurately determine the response in an industrial environment. The actual flight arrays did not receive active magnetic testing although the arrays and array extensions ("boomlets") did undergo magnetic screening (with a sensitive magnetic gradiometer) for magnetic remanence (magnetic "sniff test"). This testing is done on the flight article, and any objects (hardware, thermal blankets, etc.) installed near the end of the array, to avoid magnetic contamination near the sensor.

The entire spacecraft underwent additional testing prior to shipment to the launch site. One test ("swing test") was performed to provide an estimate of the net spacecraft magnetic moment, and another ("magnetic compatibility test") was performed to measure the magnetic field produced by systems and components when activated. The swing test, as the name implies, consists of measuring the variation in magnetic field observed by a static magnetic sensor as the spacecraft, suspended at the end of a lanyard, executed pendulum motion. This motion provides a clear periodic signal that is easily distinguished from background in an industrial facility. A rotation test was also performed, in which the suspended spacecraft was rotated in the presence of the magnetic sensor, to identify the location of magnetically "hot" components. For the magnetic compatibility test, the magnetic field was monitored as various subsystems were energized, to characterize the resultant magnetic signature. During one of these tests, we identified dc heaters in the propulsion system that had not been compensated properly; Project was able to reconfigure the operation of these heater circuits prior to shipment to reduce the stray field to acceptable levels.

V) Fluxgate Magnetometer

a. Instrument Description

The GSFC fluxgate magnetometer meets and exceeds the vector measurement requirement with a simple and robust instrument with extensive flight heritage. The MAVEN magnetometer design draws from Goddard's extensive flight experience, with over 78 magnetometers developed for space research and built at GSFC (e.g., Voyagers 1 and 2, Pioneer 11, Giotto, Lunar Prospector, Mars Observer, Mars Global Surveyor, MESSENGER, STEREO, WIND, ACE, AMPTE, TRMM, Freja, Viking, UARS, DMSP, Firewheel, MAGSAT, POGS, RBSP, and Juno). All are based on fluxgate designs developed by Mario Acuña at GSFC. The MAVEN sensors cover the modest dynamic range requirement with two instrument ranges that will be used in the Mars environment (+/- 512 nT and +/- 2048 nT full scale). The instrument also has a high range (65,536 nT full scale) that is useful in integration and test, permitting operation in ambient field in an Earth field environment without resort to magnetic shielding or nulling devices.

i. Principle of Operation

The fluxgate magnetometer is a simple, robust sensor capable of very high vector accuracy while requiring only modest resources [*Acuña*, 2002]. The principle of operation is illustrated with the help of the simplified schematic (**Figure 8**) that describes a generic, single axis fluxgate magnetometer utilizing a ring core sensing element. The sensing element is a high permeability ring formed by wrapping a thin tape of 6-81 molybdenum permalloy onto a non-magnetic Inconel hub. This material is nickel-iron alloy with about 81% nickel and 6% molybdenum content, the remainder iron, with a magnetic permeability of order 100,000.

The "fluxgate" works by driving this sensing element cyclically into saturation by exciting a toroidal winding at a drive frequency, typically about 15 kHz. The core saturation "gates" the ambient magnetic flux threading the sensing coil, as the core permeability alternates between very high, in the unsaturated state, and very low, in the saturated state. Core saturation occurs at twice the drive frequency, modulating the ambient flux at twice the drive frequency, and inducing a voltage in the sensing coil at 2f, which is amplified and passed to a synchronous detector. The

synchronous detector is essentially a lock-in amplifier, using as a reference the second harmonic of the drive frequency, all derived from a stable crystal controlled oscillator. The output of the detector is fed back to the sense coil to drive the field in the sensor to zero, which results in a sensor with very high linearity. The output voltage is linearly related to the ambient field aligned with the axis of the sense/feedback coil. Several dynamic ranges may be implemented by selection of different feedback resistors using field effect transistors to perform the switching function.

A vector instrument (**Figure 9**) incorporates three single axis analog circuits like that shown schematically in **Figure 8**, or possibly four if a redundant axis is included. The three component (x, y, z) analog outputs are sampled by dedicated 16-bit Analog-to-Digital Converters (ADC) which are controlled by, and read by, a digital processor that formats the data for transfer to the PFPDPU, along with housekeeping data (temperatures, voltages, current measurements).

The MAVEN sensor (**Figure 10 and 11**) utilizes two ring core sensing elements, each of which sits inside of a pair of nested sense/feedback coils. This design uses the pair of orthogonal sense/feedback coils to detect both components of the magnetic field in the plane of the ring core, and to null the field in the plane of the ring core. Since each sensor element measures the field in two orthogonal directions, one may either have a redundant measure of the field along one axis or one may simply drive the redundant sense/feedback coil to null with the output from the companion sensor. The MAVEN magnetometers use this approach to null the field along the redundant axis. This design achieves superior linearity in strong fields relative to designs using single axis sense/feedback coils and it uses only two ring core sensing elements instead of the three required for a vector instrument otherwise. Each sensor assembly (**Figure 12**) is permanently mated to an optical cube that defines the reference coordinate system for the sensor.

ii. Analog Design

The FGM electronics (analog and digital) for each magnetometer are mounted in a single card frame in the PFP stack (**Figure 13**). The thermal controllers for the sensors are mounted back-to-back on a small circuit board stiffener (**Figure 14**) mounted elsewhere in the PFP (instrument interface board) to avoid the possibility of interference with sensitive analog circuitry. The MAVEN

magnetometer electronics were developed with many of the same electronics parts used for the Juno instrument, which was built to operate in a more demanding radiation environment; as such, the MAVEN instrument substantially exceeds the mission radiation requirement. The sensor assembly is passive and radiation tolerant.

A common drive circuit in the analog electronics drives the two sensor ring cores into saturation at a using a dedicated toroidal winding on each ring core. The ambient magnetic field in each sensor is sensed by synchronous detection of the second harmonic of the drive frequency, the presence of which reveals an imbalance in the response of the permeable ring core due to the presence of an external field [*Acuña*, 2002]. As with any fluxgate, care must be taken to insure that the spacecraft does not generate interference at harmonics of the drive frequency which could confuse the signal attributed as an ambient magnetic field. The two magnetometers operate independently, and to ensure that one does not interfere with the other, they are driven at different frequencies derived from the master clock. Flight model 1 (FM1) uses a drive frequency of 15.2 kHz, and flight model 2 (FM2) uses a drive frequency of 16.3 kHz. This results in ample separation of the second harmonic frequencies (30.4 kHz for FM1, 32.5 kHz for FM2).

The appropriate instrument dynamic range is selected, automatically, by range control logic within the field programmable gate array (FPGA), resulting in autonomous operation through the entire dynamic range. All range and instrument control functions are implemented in hardware. The FGM powers up in operational mode autonomously, sending telemetry packets to the spacecraft C&DH immediately without need of further commands. A limited command set allows us to tailor the science and engineering telemetry to available resources (via averaging and decimation of samples or packets) and to uplink changes in the parameters that control various functions as desired.

Power and Thermal Interface

Each magnetometer sensor board receives power from the PFDPU. There are two magnetometer boards in the MAVEN implementation and each board receives an independent power service from the PFDPU in order to maintain hardware redundancy. The magnetometer electronics requires +/-13V from the PFDPU service. The MAG electronics uses local linear regulators to produce the required internal voltages for analog VREF (+11.4V), current source (-8.5V), sensor analog to digital converters (+5V

and -5V), and digital logic levels (+3.3V and +2.5V). There is no EMI filter on the MAG board for the +/-13V power supplied to MAG; this function is provided by the PFDPU power service.

The two magnetometer AC heater circuits require separate +28V supplies (+24V to +36V) and operate independently and autonomously from the sensor electronics. These power lines pass through the PFP but are powered independently of the PFP so that the MAG sensors are supplied with operational and survival thermal power regardless of the state of the PFP. Each AC heater circuit operates autonomously when the nominal spacecraft bus unregulated power is applied and requires no commands or external configuration. The heater pulse width modulator (PWM) starts to activate at approximately +30C and continues to increase power as the measured temperature drops to approximately -15C, at which point the heater is fully on. The maximum power dissipated in the 80Ω heater is dependent upon the (unregulated) power supply voltage.

The heater circuitry resides on a daughterboard resident on the power supply circuit board in the PFDPU; it is physically separated from the MAG sensor electronics. A simplified block diagram of the heater circuit is shown (**Figure 15**). The AC heater contains a transformer-coupled input that receives 3.3V level logic pulses from the DPU at a frequency of 131 kHz and a duty cycle of approximately 50%. This is used to synchronize the AC heater pulse width modulation (PWM) circuitry to the PFDPU clock. In the event that AC heater circuit power is on and the DPU clock is not present, an on-board oscillator set close to the sync frequency will operate the PWM circuit. When the PFDPU is active, the heater excitation frequency is synchronized to the PFDPU clocks. This is done to minimize interference with other sensors (principally the Langmuir probe) on the payload.

Each magnetometer heater circuit provides a transformer-coupled heater monitor as an analog output to the spacecraft. This service is provided in order to gain visibility into heater operation at times when the PFP (and MAG) is powered off. The voltage output of the heater monitor is proportional to the power dissipated in the 80Ω sensor heater resistance, providing an indirect measurement of sensor temperature that is available in spacecraft telemetry.

iii. Digital Implementation

The MAG electronics requires only simple logic and does not require the capability and complexity of a microprocessor or software; it utilizes a single, low-power Field Programmable Gate Array (FPGA). The required logic is contained within a single radiation-hard Aeroflex UT6325 FPGA with +3.3V I/O. This design closely follows the Juno implementation, for which a very robust, radiation tolerant instrument was required. This FPGA provides an ample logic capability as well as internal radiation-hard memory. Aeroflex UT54ACS14E Schmitt-trigger inverters are utilized for signals that interface to the PDFPU.

MAG receives serial commands from the PFDPU digital control board (DCB) and returns telemetry to the PFPDPU for further processing and/or transfer to the spacecraft command and data handling (C&DH) processor. The MAG board receives an 8.388 MHz clock (HFCLK) from the PFDPU (2^23 = 8,388,608 Hz) which provides the global clock used by the FPGA. A derivative of this frequency is output to the analog sensor readout portion of the circuitry and utilized for resonant tuning of the magnetometer.

The 1.048 MHz CMD_CLK signal supplied by the DCB is used to shift in the CMD data from the DCB. The shift register outputs are synchronized internally to the main FPGA MAG_OSC clock prior to use by the MAG Command Processor logic. The MAG has several commands associated with instrument operation but does not require commands at startup to function. MAG does, however, require HFCLK and CMD_CLK to produce science telemetry in the nominal operating mode. The CMD_CLK is resynchronized to the internal HFCLK prior to use by the telemetry processor.

1. Data Modes

Each MAG electronics board communicates independently with the PFDPU, immediately upon application of power, and receipt of clock, without need for commands of any kind. The MAG telemetry consists of a block of telemetry sent every second to the PFDPU for further processing and/or transmission to the spacecraft. The MAG uses this single telemetry format to communicate science and engineering data to the PFDPU. This telemetry format consists of header information

(synchronization pattern, frame counter, spacecraft time information, and MAG status) as well as a block of science measurements (three components of the vector magnetic field in sensor coordinates at 32 vector samples per second) and a block of analog and digital housekeeping information. Upon receipt, and subject to ground command, the PFDPU selects a portion of this telemetry for retransmission to the spacecraft and ground, tailoring the output to meet telemetry allocations and science requirements.

The PFDPU may perform averaging and decimation of the native 32 vector samples/sec telemetry to achieve a desired telemetry allocation. Thus sample rates of 32, 16, 8, 4, 2, 1 vector samples/sec are available (independently) for each magnetometer. The PFDPU may also implement a simple 8-bit differencing scheme that offers a factor of two data compression, exclusive of the uncompressed header, for each instrument (independently). In our implementation, this data compression scheme is lossless: if any of the differences exceed the 8-bit dynamic range allocated, the uncompressed packet is transmitted instead. In both cruise and the Mars environment, this will occur (and indeed has occurred) very infrequently. The difference mode may be selected by ground command, relayed via the PFDPU; it has been used liberally throughout cruise to Mars.

2. Range Change Algorithm

Each MAG electronics card provides logic for autonomous operation of the magnetometer sensor, choosing an appropriate dynamic range (512, 2048, or 65,536 nT) depending on the environmental field. Alternatively, the instrument dynamic range may be commanded (manual mode) via an instruction passed to MAG via the PFDPU. Automatic range control is designed to work with minimal mathematics operations (lacking a microprocessor) by simple inspection of the three components of the measured magnetic field. The algorithm provides adequate hysteresis to prevent multiple transitions ("toggling") in the vicinity of a threshold and uses a "look back" period to prevent multiple transitions during spacecraft rolls; it is based on the Juno algorithm.

Each MAG allows a change of dynamic range only at a packet boundary (once per second). The instrument range reported in the packet header thus represents the dynamic range of all samples

acquired in the corresponding one second interval. The MAG will range up (increasing dynamic range, decreasing sensitivity) in order to prevent saturation of individual axes. The ranging algorithm keeps track of how many times a measurement (in each component) exceeds a ranging threshold (**Figure 16**); if this count exceeds a (programmable) threshold, the instrument will range up at the next opportunity (packet boundary). This feature provides some noise immunity in that it makes it unlikely that a spurious measurement, or a few spurious measurements, will inadvertently trigger a range change.

Each MAG will range down (decreasing dynamic range, increasing sensitivity) to preserve as much measurement resolution as possible. Ranging down works in a similar manner, but threshold comparisons are made over a "look back" interval that is designed to encompass at least one spin period. This is used to prevent undesired range changes that would otherwise occur when all three components of the field drop below a threshold for only a portion of the spacecraft spin period. The MAVEN spacecraft is not a spinning spacecraft, but it is required to perform rotations about spacecraft principal axes from time to time to satisfy instrument calibration requirements.

The 512 nT dynamic range is anticipated to satisfy measurement requirements throughout the vast majority of the mission, including the "deep dip" campaigns that bring the spacecraft to lower altitudes. In this range, the 16 bit quantization provides more than adequate measurement resolution (+/- 0.015 nT), and a greater dynamic range would be required only if the periapsis during one of the deep dips occurred over a specific latitude and longitude corresponding to the most intensely magnetized site in the Mars crust. This is unlikely to occur unintentionally but the instrument has the capability to optimize the dynamic range should the very strongest field be encountered at periapsis during a deep dip.

iv. Radiation Environment and Parts Engineering

The MAVEN electronics parts radiation requirement is met by parts that are radiation tolerant to TID 13 krads (Si) @ 100 mil Al. Additionally, electronic parts are required to meet a LET threshold against latchup and SEE of 75 MeV-cm^2/mg (or undergo further testing). Additional

details are available in the MAVEN Environmental Requirements Document, MAVEN-SYS-RQMT-0010. The MAVEN electronics design and implementation closely follows that of the Juno magnetometer investigation [*Connerney et al.*, 2014], which was designed for a more severe radiation environment (50 krads TID with a radiation design margin of 2). The MAVEN magnetometers were built from the Juno parts list and as such greatly exceed the MAVEN radiation requirement.

v. Performance

Performance of the magnetometers was monitored throughout the test program (Table) using a series of calibration procedures repeated before and after significant environmental tests. These calibration procedures are discussed below and in more detail in *Connerney et al*., [2014]. FM1 preceded FM2 through development and thus had a more extensive series of calibrations.

A sensor with linear response may be characterized by the sensor model:

$$[B] = [A] \begin{bmatrix} s_1 (c_1 - o_1) \\ s_2 (c_2 - o_2) \\ s_3 (c_3 - o_3) \end{bmatrix}$$

Where the true field vector [B] may be expressed as a linear combination [A] of the sensor response; here [A] is a nearly diagonal 3 by 3 matrix. The three components of the sensor response in counts (c_i) are corrected for small offsets (o_i) and scaled to magnetic units with scale factors (s_i). In practice we use near-unity s_i that are slight corrections to the nominal scale factors. The matrix A is often called the "orthogonality matrix" and it is a function of the sensor construction and alignment to the reference cube; it is used to express the measured field in the coordinate system defined by the reference cube normal vectors. We compared calibrations performed prior to and after vibration tests to demonstrate alignment stability to 0.03º or better. Similarly, across all environmental tests, scale factors for both instruments varied by less than 4×10^{-4}.

651 Table 1: Schedule of calibration activities throughout the environmental testing program.

652

FM1	Thinshell	Zeros	MAGSAT
23Feb12		√	√
28Feb12	√	√	√
12Mar12	√	√	√
14Mar12	√	√	√
March 13-21 Thermal Balance			
18Apr12		√	√
April 21-23 Vibration			
19Apr12	√	√	√
25Apr12	√	√	√
27Apr12			
May 2-10 Thermal Cycles			
14May12	√	√	√
15May12		√	√
FM2			
13Mar12	√	√	
March 13-21 Thermal Balance			
21Mar12		√	√
20Apr12	√	√	√
April 21-23 Vibration			
25Apr12	√	√	√
30Apr12			
May 2-10 Thermal Cycles			
15May12	√	√	√

653
654
655 vi. Test Program
656
657 The MAVEN instruments followed the GSFC MAG group's standard laboratory setup and test
658 procedure. The sensor bobbins and sensor assembly are thermally cycled over a wide temperature
659 range for mechanical stress relief. The sensors are thermally cycled once from +75 ºC to -35 ºC

followed by 12 cycles from +60 ºC to -20 ºC. The magnetometer electronics progress through resonant tuning of the analog input circuitry and frequency response verification, followed by voltage, temperature, and frequency margin testing (VTFMT) in the lab. This involves comprehensive functional testing at hot and cold temperature extremes (+80 ºC to -40 ºC) while varying voltages and frequencies over their margined envelopes. The electronics and sensor were also assayed for biological contamination prior to delivery.

The magnetometer electronics were integrated to the main electronics box of the PFP and experienced environment tests as part of the PFP instrument suite including thermal vacuum, thermal balance, the full array of electromagnetic compatibility tests, and vibration. Before and after each test element, comprehensive end-to-end functional tests were performed to provide system-level baselines for MAG. While it is not feasible to perform accurate magnetic calibrations without access to the magnetic test site, functional performance and sensor noise levels were established within two four-layer Mu-metal shield cans. These shielded enclosures were designed to protect the sensors from physical damage throughout integration with the PFP at the University of California, Berkeley, and later in the ATLO environment at Lockheed Martin's Waterton Canyon facility in Denver. Each of the multilayer Mu-metal shielded enclosures was fitted with a computer-controlled tri-axial coil system that was used inside the shield cans for both AC and DC stimuli. This allowed full functional verification throughout integration and test at Lockheed's facility. The magnetometer sensors were to be mounted, eventually, at the outer end of the solar panels, but throughout much of ATLO the solar panels are not physically present. Therefore the sensors were mounted atop the spacecraft buss, within their protective enclosures, to facilitate integration and test while awaiting final assembly.

vii. Calibration

Calibrations of the MAVEN MAG instruments were performed on numerous occasions at system and subsystem levels. We used subsystem level calibrations on the FGMs to establish performance characteristics well in advance of system level calibrations. Later in development, when the Flight Models (FMs) were available, system level calibrations were performed before and after each element of the environmental test program (e.g., vibration, thermal vacuum) to establish that exposure to extreme environmental conditions did not alter the instrument response to magnetic fields. At the system level,

692 our reference coordinate system is determined by the non-magnetic reflective optical cube affixed to
693 each sensor. These small optical cubes (0.5 inch on a side) are fabricated to 10 arcsec orthogonality and
694 all cubes were independently measured by the optics branch at GSFC. The magnetometer response is
695 determined relative to this cube. Calibrations relative to the optical cube include both intrinsic sensor
696 performance and the stability of the mechanical system that serves to bind all elements to each other.
697
698 Magnetic calibrations were performed at the GSFC Mario H. Acuña (MHA) Magnetic Test Facility
699 (MTF), a remote facility located adjacent to the GSFC campus. The MTF includes a 22 foot diameter
700 Braunbeck coil system (building 303), and associated control (building 304) and reference (building
701 309) structures, as well as other facilities. The 22 foot facility is sufficient to calibrate magnetometers to
702 better than 100 parts per million (ppm) absolute accuracy for applied fields in all directions and field
703 magnitudes up to about 1 Gauss. An independent measurement of applied magnetic fields is provided by
704 Overhausen Proton Precession magnetometers (reference magnetometer) placed near the unit under test.
705 The Proton Precession magnetometers provide an absolute measurement of the applied field over the
706 dynamic range of about 20,000 nT to 1.2 Gauss (120,000 nT). The facility is operated in a closed loop
707 with a remote reference vector magnetometer to null variations in the earth's field so applied fields may
708 be held constant to a fraction of a nT over the duration of a calibration sequence.
709
710 Two independent methods were used to calibrate the MAVEN magnetometers. The vector fluxgates are
711 calibrated in the 22' facility using a method ("MAGSAT method") developed by Mario Acuña for
712 calibration of the magnetometer flown on the MAGSAT mission. This technique uses precise 90 degree
713 rotations of the sensing element and a sequence of applied (facility) fields to simultaneously determine
714 the parameters of the magnetometer model response as well as a similar set of parameters that describe
715 the facility coil orthogonality [*Acuña,* 1981; a more accessible reference is *Connerney et al.,* 2014]. The
716 method takes advantage of the accuracy with which the orientation of the sensor (reference optical cube)
717 may be determined via autocollimation with a set of precision theodolites or alternately laser
718 autocollimators. We used a pair of T-3000 theodolites permanently affixed to the coil facility structural
719 members for this purpose. The method uses a sequence of applied fields of known magnitude aligned
720 with the coil system symmetry axes (north-south, east-west, up-down) with the sensor oriented in a
721 minimum of 3 orientations, as determined above, representing precise 90 degree rotations from the

initial orientation. All of the elements of the linear sensor response may be determined by inverting the resulting overdetermined linear system [*Connerney et al*, 2004].

The second calibration method, developed by the DTU researchers (called the "thin shell" method, alternately the "Orsted" method) uses a large set of rotations in a known and stable field to obtain much the same instrument parameters, subject to an arbitrary rotation [*Risbo et al.,* 2002]. This method can be performed at a suitable (i.e., magnetically quiet) location using the earth's field as a reference, simply by making a sufficient number of measurements of the vector field measured by the sensor in many orientations relative to the ambient field – thus the name: "thin shell". This method also employs a Proton Precession reference magnetometer to measure the ambient field magnitude and account for any variations in the field during the test. Of course, this method can also be employed in a magnetic test facility at any desired field magnitude within the dynamic range of the facility. So we have also performed calibrations of the MAVEN magnetometers in our facility at several applied field magnitudes (which we call "thick shell" or nested thin shell calibrations) using this method; these may be performed relatively quickly.

The "thin shell" method by itself determines the magnetometer sensor response in an unknown coordinate system – an "intrinsic" coordinate system of the magnetometer sensor – the orientation of which needs to be determined by other means. This is equivalent to stating that the parameters of the linear sensor model may be determined subject to an arbitrary rotation, or, that only the symmetric part of the sensor response matrix is established via a "thin shell" calibration.

Sensor zero offsets are determined in the magnetic facility by physically reversing the sensor in a weak field, or by rotating the sensor in a weak (or zero) field. This may be done either in the center of the coil system, operated in nulling mode, or inside of a suitably demagnetized, multi-layer mu metal shield can.

b. In-Flight Calibrations

In-flight calibrations are designed to monitor stability of magnetometer offsets and to provide a capability to diagnose and monitor spacecraft-generated magnetic fields. In most applications, the magnetic sensors are fixed in the spacecraft reference frame, and a constant magnetic field in the sensor (sensor offset or bias) is indistinguishable from a constant ("static") spacecraft-generated magnetic field. Thus it is common practice to lump them together and estimate the sum of the sensor offset and static spacecraft magnetic field. This may be done by performing spacecraft rotations in the environmental magnetic field.

i. Fluxgate Zeros and Static Spacecraft Field Determination

The mission plan allows for magnetic calibration maneuvers (roll maneuvers) that are scheduled to occur during the science collection phase approximately every other month, interleaved loosely with calibration maneuvers scheduled for the UVS investigation on a similar cadence. Two MAG calibration roll activities have already been conducted during cruise operations. Another set of MAG calibration maneuvers is scheduled to occur during transition orbit phase, and subsequent maneuvers will be scheduled throughout science phase. Care is taken to schedule the MAG calibration maneuvers to occur when (where) the spacecraft is more likely to experience a relatively benign environment – i.e., times and places where the magnetic field is more likely to be relatively quiet and not large in magnitude. For example, MAG calibrations will avoid periapsis where large variations in the magnetic field are expected and regions of near Mars space characterized by large field fluctuations (e.g., magnetosheath).

The periodic MAG calibration sequences (MAGROLLS) are designed to provide ~12 rotations about one axis, followed immediately by another ~12 rotations about a second sc axis. These execute at ~2 degrees per second rotation rate and each set of 12 rotations require about 42 minutes to complete. Prior to execution of the maneuver, a command is sent to reduce the spacecraft battery state of charge (SOC) to 80%, which effectively shuts off the solar arrays for the duration of the maneuver. This is done to eliminate the possibility of variable fields associated with solar array circuitry that might arise under variations of solar illumination angle (the subject of another set of in-flight tests). **Figure 17** shows the magnetic field measured during MAVEN's second MAGROLL sequence performed on day 183, 2014. A set of rotations about two different axes is

sufficient to uniquely determine the combined sensor offsets/spacecraft field as long as the spacecraft magnetic field does not vary during the maneuvers. The rolls occur about the spacecraft principal moments of inertia, which depend on deployments, and are not aligned with the spacecraft payload coordinate system. For simplicity we refer to the roll axis closest to the spacecraft z axis as the "z axis" roll, and that closest to the x axis as the "x axis" roll. Inspection of the vector field during these rolls demonstrates that the rotation axes are not closely aligned with the spacecraft payload axes in the cruise (stowed) configuration.

We will use the term "offset" to describe the combined sensor zeros and spacecraft static field in what follows. We use a statistical least-squares estimation algorithm described by *Acuña* [2002] to estimate offsets. This method was developed to estimate offsets using the Alfvenic properties of the solar wind, that is, the observation that magnetic field variations in the solar wind tend to be variations in angular direction, preserving the magnitude of the field. The method works very well applied to spacecraft rolls where the variations in the vector field ought to preserve the field magnitude as well. The offset vector ($\boldsymbol{O}$) is obtained from a series of vector measurements (i = 1,2,3,…n) of the magnetic field,

$$\boldsymbol{O} = \left[\, 0.5 \left(\boldsymbol{B}_i + \boldsymbol{B}_{(i+l)}\right) \Delta \boldsymbol{B}_i \,\right] \left[\, \Delta \boldsymbol{B}_i \,\right]^{-1}$$

Where the difference $\Delta \boldsymbol{B}_i = \boldsymbol{B}_i - \boldsymbol{B}_{(i+l)}$ may be formed using sequential measurements of the vector field (l = 1) or measurements separated by l samples, chosen to provide a suitable vector difference $\Delta \boldsymbol{B}_i$, compared to measurement noise or instrument quantization step size, but not so large that variations in the field magnitude over l samples arise often. Applied to spacecraft rolls, l should be chosen to provide difference point pairs over a small fraction of a roll period. The inverse of the 3 x n matrix $[\, \Delta \boldsymbol{B}_i \,]$ is obtained using the singular value decomposition method [*Lanczos*, 1961]. Mario Acuña obtained the result above simply by observing that differences in the measured vector field during a pure rotation of the field ought to be orthogonal to the ambient field, which is simply the measured field minus the offset. *Leinweber et. al*. [2008] showed that this result may also be obtained by assuming that variations in the field magnitude are uncorrelated with the variance in differences of the three components. Simply stated, if the offsets are properly estimated, the measured field magnitude will not evidence a spin modulation as the spacecraft rotates [see also *Auster et al.,* 2002]. **Figure 18** shows the result of the offset estimation methodology applied to the

second MAGROLL maneuver obtained in cruise, which provides an estimate of the offset appropriate to that time (and the state of the spacecraft at that time). The MAVEN spacecraft will execute these maneuvers periodically, approximately every other month, as conditions dictate to monitor stability of the offsets over time. The current plan calls for these observations to be obtained in relatively low noise environments (solar wind, magnetotail), access to which is dictated by the orbital evolution and to some extent solar wind conditions. The latter are unpredictable on a time scale relevant to mission operations planning.

ii. Spacecraft-generated Magnetic Fields

Operation of the science instruments during cruise to Mars provided an opportunity to acquire instrument and subsystem calibration and performance data, exercise operations processes that will be required on orbit, and gain experience operating the instruments and the spacecraft. Operation of the magnetometers during the cruise phase also provides the first magnetic measurements of the spacecraft and systems, fully integrated and functioning in flight configuration, and operating in a low field environment. During cruise we noted spacecraft-generated magnetic fields of low amplitude associated with a few subsystems, notably thrusters (used infrequently after orbit insertion and orbital period reduction), reaction wheels, and the power subsystem (solar array circuits). The latter two sources are capable of producing fields of ~1 nT at the sensor locations, under some circumstances. The Project is actively investigating mitigation strategies to reduce or eliminate these effects during routine science operations.

The magnetic fields associated with the four reaction wheel assemblies appear at the (variable) frequency of operation of the individual wheels when their speed falls within the passband (0-16 Hz) of the magnetometers. The periodic signal from these sources is typically of low magnitude (0.1 – 0.2 nT) but has been observed to increase in magnitude at very low reaction wheel speeds. Project is currently evaluating a proposal to bias the reaction wheel speeds to higher RPMs during science operations to shift the interference above the magnetometers passband (or to as high a frequency as is practical).

We also observed variations in magnetic field associated with solar array operation that we have identified with switching of one or more circuits residing on the outer solar array panels. We originally detected a step variation if the field at the –Y sensor location (~1 nT) and the +Y sensor location (~0.5 nT) during early cruise that occurred when the solar arrays were essentially switched off via a command to reduce the state of charge of the batteries. An additional in-flight test is planned prior to the start of science operations that will excite individual circuits on the outer panels so we can uniquely identify the source and correct the field, analytically, using spacecraft telemetry that identifies changes in switch state.

VI) Operations and Data Processing

a. Science Orbits Operations

The magnetometers were powered again on shortly after the Mars Orbit Insertion (MOI) maneuver and they are to remain on throughout the mission. Orbital operations then largely of managing the instrument sample rate to conform to the instrument telemetry allocation and planning spacecraft maneuvers designed to diagnose and track any changes in spacecraft magnetic field and/or instrument offsets. In late cruise and during early science operations, both instruments are being operated at the same sample rate to assist in this process.

Current plans call for the magnetometer to sample at the high (32 vectors/s) rate throughout periapsis (altitude less than 500 km) and at lesser rates throughout the rest of the orbit, subject to the (time-variable) telemetry allocation. Telemetry allocations change throughout the mission subject to practical limitations, such as the Earth-Mars distance and the number and frequency of downlink opportunities afforded the Mission. In addition, the PFDPU collects and stores magnetometer data at the highest rate continuously, and holds this data, along with that from the particle instruments and the Langmuir and Plasma Wave Investigation, in memory aboard the spacecraft. This data ("burst mode") is available for downlink upon command, after an examination of the "survey" data already downlinked. The concept allows the science team to decide how to allocate precious telemetry resources (downlink at high time resolution the data that's most interesting)

retrospectively, after a brief examination of the time series data downlinked at a lesser rate earlier. Eventually the on-board memory is written over, making room for new burst mode observations.

b. Data Processing

Ground processing of magnetometer data is performed routinely at GSFC following downlink and transmission to the Science Data Center (SDC) at the University of Colorado, Boulder. An automated script at GSFC searches the database at the SDC for data files that have yet to be downloaded, executing hourly. Files identified as such are pulled to the MAG operations computer automatically and queued for immediate processing.

The MAG data processing is responsive to the need for rapid turn-around, since other instruments require magnetic field vectors in their preliminary analysis, by design before spacecraft supplementary engineering data is available for archive processing. A preliminary MAG data processing pipeline (**Figure 19**) executes prior to receipt of reconstructed spacecraft ephemeris (NAIF SPK kernels) and attitude information (NAIF C-kernels) necessary for archive processing, and without benefit of engineering telemetry that may be necessary for detailed analysis. Preliminary processing is conducted to assess the health and safety of the instrument, producing time series magnetic field vectors in either sensor or spacecraft payload coordinates that are useful in diagnosing instrument offsets and spacecraft-generated magnetic fields.

A similar but more comprehensive archive processing pipeline (**Figure 20**) incorporates reconstructed spacecraft ephemeris and attitude information, and any supplementary spacecraft engineering information, producing magnetic field vectors, and spacecraft position vectors, in a variety of coordinate systems of interest.

Both processing pipelines utilize the same code which is designed to retain the ability to process data when supplementary data is lacking for a complete analysis. The data flow is designed to be extremely flexible in the ability to assimilate unanticipated observations, such as engineering telemetry that may be desired for analysis, and not anticipated early in the mission. This facility is

implemented by utilizing a decommutated telemetry file that passes data to the main processing program in a text "keyword = value" format, originally developed for the Mars Observer and Mars Global Surveyor Projects.

i. Telemetry De-commutation

Raw binary MAG packets are checked for errors and decommutated using a bit map appropriate to the instrument mode (sample rate, differencing scheme if elected). Each data packet contains sufficient information within its header to allow processing of the data that it contains, from a magnetometer only perspective (i.e., excluding any spacecraft engineering data that may be required). The decom program produces a decommutated telemetry file (".dtl" extension) that is an ASCII stream of "keyword = value" pairs, utilizing a text format similar to that employed by JPL's NAIF text kernel readers.

ii. MAG Packet Processing

MAG packet processing operates on the dtl input files, converting instrument counts to magnetic field in nanoteslas, and engineering measurements in counts to engineering units, using calibration files for the instruments and conversion coefficients for engineering quantities (currents, temperatures, voltages, etc.). A SCLK (spacecraft clock) conversion file, provided by NAIF, is required to convert spacecraft clock words to Coordinated Universal Time (UTC), and a leapseconds kernel file ("leap.ker"), also provided by NAIF, is required to maintain accuracy of UTC time conversions. The input files may contain sensor data from either or both of the magnetometers, depending on whether the two (independent) data streams are merged, and as is the case in archive processing, may contain supplementary spacecraft engineering data (e.g., solar array currents, solar array switch states, etc.) for use in spacecraft magnetic field mitigation.

Archive processing adds access to reconstructed spacecraft ephemeris (SPK) and attitude information (C-kernels) that are delivered somewhat later than the instrument science data on a schedule dictated by Project. The Project currently envisions a weekly delivery of bested C-kernels, which are pieced together from a set of many smaller files that contain overlapping data in places,

abundant data gaps, and retransmission duplicates. The C-kernels are required to render spacecraft position and magnetic field vectors in the desired coordinate systems. These vectors appear in Cartesian coordinates on output records, one record per observation, at the highest time resolution available, for science data archive. Archive processing may also include spacecraft supplementary engineering data, merged with the instrument science data in dtl files, should that be necessary in processing a correction for time-variable spacecraft-generated magnetic fields. Where necessary engineering data is not available with the required time cadence, interpolation of the engineering data may be required; if interpolation is not feasible, as an alternative, the magnetic field vectors may be averaged and resampled, if necessary. Static spacecraft magnetic fields are compensated via subtraction of a constant (for example, determined from a previous spacecraft roll maneuver, or MAGROLL calibration sequence) that is passed to the analysis program via the input dtl file.

iii. NAIF Kernel Utilities for Ancillary Engineering

The only component on the spacecraft that articulates is the Articulated Payload Platform (APP), since the spacecraft solar arrays and the high gain antenna are all fixed. A moving component or subsystem is a potential source of a variable spacecraft magnetic field, if it has a significant magnetic moment. The APP will be calibrated after deployment (post-MOI) by taking observations of celestial objects in different directions, and before science operations begin, an in-flight magnetic compatibility test will be performed. This test consists of cycling the APP through rotations about the two articulation axes while the magnetic sensors record the magnetic field. In the event that the APP produces a variation in the magnetic field sensed by the magnetometers, an attitude kernel (C-kernel) for the APP will be available for use by the team in applying a correction.

iv. Spacecraft Magnetic Field Mitigation

A static spacecraft magnetic field or instrument offset is measured via periodic spacecraft roll maneuvers and eliminated in data processing either via adjustment of sensor zeros in the instrument calibration file or by insertion of an offset variable in the decommutated telemetry file for each sensor. As of this writing we anticipate that a dynamic correction will be implemented to compensate for the field produced by the solar array, using spacecraft telemetry on switch states and

measurements of the current produced by illumination of the arrays. Implementation of this correction will follow analysis of the in-flight tests planned for execution in the near future. The engineering telemetry necessary for this correction will be passed to the processing program via augmentation of the dtl file. We also anticipate archiving the reaction wheel speeds along with the magnetometer data to avoid confusion with environmental phenomena.

c. Standard Data Products

For immediate use by the science team, and other instrument teams, we provide a quicklook product that consists of time-ordered records of magnetic field vectors in nanoteslas, rendered in spacecraft payload coordinates, along with browse products that are useful in identification of intervals of special interest. These files contain magnetic field processed with a static spacecraft field approximation, but do incorporate the full sensor zeros, calibration scale factors, and sensor orthogonality matrix conversion. These quicklook products are intended for preliminary analysis and planning purposes and are not intended for science archive.

Archive products are produced in a variety of coordinate systems when final reconstructed spacecraft ephemeris and attitude information is available. These include a planet-centered ("pc") coordinate system, rotating with Mars (z aligned with the spin axis) and with the x axis through the Mars IAU prime meridian; and a sun-state ("ss") coordinate system wherein the primary reference vector (x axis) points from the object (Mars) to the sun and the secondary reference vector (y axis) is in the Mars orbit plane (approximately opposite to orbital motion) such that the z axis is northward. Both of these coordinate systems are also available with respect to any other body ("object") of interest, for example, the satellites Phobos and Deimos.

Science archive products are pushed to the SDC on a regular schedule.

VII) Summary

The MAVEN magnetic fields investigation will provide accurate vector magnetic field observations throughout all phases of the mission at sample rates of up to 32 vector samples/s, depending on telemetry allocation. The instrumentation provides two-sensor vector measurements for spacecraft

magnetic field mitigation and complete hardware redundancy for risk mitigation. Magnetic field vectors are provided in-flight for use by other payloads in optimizing data collection and telemetry utilization. Spacecraft maneuvers (MAGROLLS) will be performed during science operations approximately every two months to monitor spacecraft fields and sensor offsets, and a series of additional in-flight tests have been performed to diagnose and correct for small-amplitude spacecraft-generated magnetic fields. These data, together with the synergistic particle observations acquired by the PFP instrumentation, and observations of plasma waves, ultraviolet emissions, and mass spectrometry, will form the foundation of a comprehensive study of the Mars atmosphere and its evolution.

1012 References

1013

1014 Acuña, M. H., (1981). MAGSAT – vector magnetometer absolute sensor alignment determination.
1015 NASA Technical Memorandum, 79648.

1016 Acuña, M. H., (2002). Space-based magnetometers. *Review of Scientific Instruments* **73**, No. 11, 3717-
1017 3736.

1018 Acuña, M. H., Connerney, J. E. P., Wasilewski, P., et al. (1998). Magnetic field and plasma observations
1019 at Mars: Initial results of the Mars Global Surveyor Mission, *Science,* **279***,* 1676-1680.

1020 Acuña, M. H., Connerney, J. E. P., Ness, N. F., et al. (1999). Global distribution of crustal magnetism
1021 discovered by the Mars Global Surveyor MAG/ER Experiment. *Science* **284**: 790-793.

1022 Acuña, M. H., Connerney, J. E. P., Wasilewski, P., *et al.* (2001). The magnetic field of Mars: Summary
1023 of results from the aerobraking and mapping orbits. *Journal of Geophysical Research* **106**: 23403-
1024 23417.

1025 Andersson, L. A., R.E. Ergun, G.T. Delory, A. Erickson, The Langmuir probe instrument on MAVEN.
1026 *Space Sci. Rev.* (2014, this issue).

1027 Andersson, L., et al. (2010). The Combined Atmospheric Photochemistry and Ion Tracing code:
1028 Reproducing the Viking Lander results and initial outflow results. *Icarus* **206**(1): 120-129.Auster, H.
1029 U., fornacon, K. H., Georgescu, E., Glassmeier, K. H., and Motschumann, U. (2002). Calibration of
1030 fluxgate magnetometers using relative motion, *Meas. Sci. Technol.* **13**, 1124-1131.

1031 Barabash S., Fedorov A., Lundin R., Sauvaud J. A. (2007), Martian atmospheric erosion rates, *Science*
1032 **315**(5811): 501-503.

1033 Bertaux, J. –L., F. Leblanc, O. Witasse, E. Quemerais, J. Lilensten, S.A. Stern, B. Sandel, O. Korablev,
1034 (2005) Nature **435**, 790-794. doi:10.1038/nature03603.

1035 Bertucci, C., Mazelle, C., Crider, D. H., Vignes, D., Acuña, M. H., Mitchell, D. L., Lin, R. P.,
1036 Connerney, J. E. P., Reme, H., Cloutier, P. A., Ness, N. F., Winterhalter, D. (2003), Magnetic field
1037 draping enhancement at the Martian magnetic pileup boundary from Mars global surveyor
1038 observations, *Geophys. Res. Lett.* **30**(2).

1039 Brain, D. A., Space Sci. Rev. **126**, 77-112 (2006).Brain, D. A., J. S. Halekas, L. M. Peticolas, R. P. Lin,
1040 J. G. Luhmann, D. L. Mitchell, G. T. Delory, S. W. Bougher, M. H. Acuña, and H. Rème (2006), On
1041 the origin of aurorae on Mars, *Geophys. Res. Lett.*, 33, L01201, doi:10.1029/2005GL024782.

1042 Brain, D.A., A. H. Baker, J. Briggs, J. P. Eastwood, J. S. Halekas, and T.- D. Phan (2010), Episodic
1043 detachment of Martian crustal magnetic fields leading to bulk atmospheric plasma escape, *Geophys.*
1044 *Res. Lett.*, **37**, L14108, doi:10.1029/2010GL043916.

1045 Brain, D. A., and J.S. Halekas, in *Auroral Phenomenology and Magnetospheric Processes: Earth and*
1046 *Other Planets*, ed. by A. Keiling, E. Donovan, F. Bagenal, T. Karlsson (American Geophysical Union,
1047 Washington, D.C., 2012) pp.123-132. doi:10.1029/2011GM001201.

1048 Brain, D. A., in *Atmosphere and Climate of Mars*, eds. R. Haberle, T. Clancy, F. Forget, M. Smith, R.
1049 Zurek (Cambridge University Press, 2014), in press.

1050 Breuer, D. and T. Spohn, Early plate tectonics vs. single plate tectonics on Mars: Evidence from
1051 magnetic field history and crust evolution, *J. Geophys. Res.*, submitted, 2003.

1052 Connerney, J. E. P., Acuña, M. H., Wasilewski, P. J., Ness, N. F., *et al.,* (1999). Magnetic lineations in
1053 the ancient crust of Mars, *Science* **284**: 794-798.

1054 Connerney, J. E. P., Acuña, M. H., Ness, N. F., Spohn, T., and Schubert, G. (2004). Mars crustal
1055 magnetism. *Space Science Reviews* **111**(1-2): 1-32.

1056 Connerney, J. E. P., Acuña, M. H., Ness, N. F., Kletetschka, G. *et al.,* (2005). Tectonic implications of
1057 Mars crustal magnetism. *Proceedings of the National Academy of Sciences* **102**(42): 14970-14975.

1058 Connerney, J. E. P., et al., (2014). The Juno Magnetic Field Investigation. *Space Science Reviews*, in
1059 preparation.

1060 Dong, C.F., Bougher, S.W., Ma, Y.J., Toth, G., Nagy, A.F., and Najib, D., (2014) Solar wind
1061 interaction with Mars upper atmosphere: Results from the one-way coupling between the multi-fluid
1062 MHD model and the MTGCM model, Geophys. Res. Lett., doi:10.1002/2014GL059515.

1063 Ergun, R. E., Andersson, L., Peterson, W. K., Brain, D., Delory, G. T., Mitchell, D. L., Lin, R. P., Yau,
1064 A. W. (2006), Role of plasma waves in Mars' atmospheric loss, *Geophys. Res. Lett.* **33**(14).

1065 Espley, J.R., P.A. Cloutier, D.A. Brain, D.H. Crider, M.H. Acuña (2004), Observations of low-
1066 frequency magnetic oscillations in the Martian magnetosheath, magnetic pileup region, and tail, *J.*
1067 *Geophys. Res., 109*, A07213, doi:10.1029/2003JA010193.

1068 Glassmeier, K. H., and J. Espley (2006), ULF waves in planetary magnetospheres, *Magnetospheric ULF*
1069 *Waves: Synthesis and New Directions* **169**: 341-359.

1070 Halekas, J. S., Eastwood, J. P., Brain, D. A., Phan, T. D., Oieroset, M., Lin, R. P. (2009), In situ
1071 observations of reconnection Hall magnetic fields at Mars: Evidence for ion diffusion region
1072 encounters, *J. Geophys. Res.-Space Physics* **114**.

1073 Jakosky, B. M., and R. J. Phillips (2001). Mars' volatile and climate history. *Nature* **412**(6843): 237-
1074 244.

1075 Jakosky, B., R.P. Lin, J. Grebowsky, J.G. Luhmann, D.L. Mitchell, D.A. Brain, R.J. Lillis et al., The
1076 2013 Mars Atmosphere and Volatile Evolution (MAVEN) mission to Mars. *Space Sci. Rev*. (2014,
1077 this issue).

1078 Lanczos, C. (1961) *Linear Differential Operations*, 564 pp., D. Van Nostrand, Princeton, N.J.

1079 Leinweber, H. K., Russell, C. T., Torkar, K., Zhang, T. L., and Angelopoulos, V. (2008). An advanced
1080 approach to finding magnetometer zero levels in the interplanetary magnetic field. *Meas. Sci. Technol.*
1081 **19**, 055104, doi:10.1088/0957-0233/19/5/055104.

1082 Lillis, R. J., Frey, H. V., Manga, M., *et al.* (2008) An improved crustal magnetic field map of Mars from
1083 electron reflectometry: Highland volcano magmatic history and the end of the martian dynamo. *Icarus*
1084 **194**: 575-596.

1085 Lillis, R. J., Robbins, S., Manga, M., Halekas, J. S. and Frey, H. V. (2013). Time history of the martian
1086 dynamo from crater magnetic field analysis. *Journal of Geophysical Research* **118**:1488-1511
1087 (doi:10.1002/jgre.20105).

1088 Luhmann, J. G., Russell, C. T., Brace, L. H., and Vaisberg, O. L., (1992) The intrinsic magnetic field
1089 and solar wind interaction with Mars, in *Mars,* eds. Hugh H. Kieffer, Bruce M. jakosky, Conway W.
1090 Snyder, and Mildred S. Matthews, University of Arizona press, 1090-1134.

1091 Lundin, R., et al., Space Sci. Rev. **126**, 333-354 (2006). doi:10.1007/s11214-006-9086-x.

1092 Ma, Y. J., Nagy, A. F., Sokolov, I. V., and Hansen, K. C., (2004) Three-dimensional, multi-species, high
1093 spatial resolution MHD studies of the solar wind interaction with Mars, *Journal of Geophysical*
1094 *Research* **109**, A07211, doi:10.1029/2003JA010367.

1095 Mahaffy, P. R., et al. (2013), Abundance and Isotopic Composition of Gases in the Martian Atmosphere
1096 from the Curiosity Rover, *Science* **341**(6143): 263-266.

1097 Mitchell, D., L., C. Mazelle, J.A. Sauvaud, D. Toublanc, Thocaven, Rouzaud, A. Federov, E.R. Taylor,
1098 M. Robinson, P. Turin, D.W. Curtis, The MAVEN Solar Wind Electron Analyzer (SWEA). *Space.*
1099 *Sci. Rev.* (2014, this issue).

1100 Nilsson, H., Edberg, N. J. T., Stenberg, G., Barabash, S., Holmstrom, M., Futaana, Y., Lundin, R.,
1101 Fedorov, A. (2011), Heavy ion escape from Mars, influence from solar wind conditions and crustal
1102 magnetic fields, *Icarus* **215**(2): 475-484.

1103 Nimmo, F. and Stevenson, D. (2000). Influence of early plate tectonics on the thermal evolution and
1104 magnetic field of Mars. *Journal of Geophysical Research* **105**: 11969-11976.

1105 Risbo, T., P. Brauer, J. M. G. Merayo, O. Nielsen, J. R. Petersen, F. Primdahl, and N. Olsen., (2002). Ørsted
1106 calibration mission: The thin shell method and the spherical harmonic analysis, in *Ground and In-Flight Space*
1107 *Magnetometer Calibration Techniques*, vol. ESA SP-490.

1108 Schubert G. and T. Spohn (1990) Thermal history of Mars and the sulfur content of its core, *J. Geophys.*
1109 *Res., 95*, 14,095-14,104.

1110 Schubert, G; S. C. Solomon, D. L. Turcotte, M. J. Drake, and N. Sleep (1992) Origin and thermal
1111 evolution of Mars, in *Mars*, ED: Kieffer, Hugh H; Jakosky, Bruce M; Snyder, Conway W; Matthews,
1112 Mildred S ,University of Arizona Press, Tucson, AZ, Pages 147-183.

1113 Sleep, N. H. (1994). Martian plate tectonics, *Journal of Geophysical Research* **99**: 5639-5655.

1114 Stevenson, D. J., T. Spohn, and G. Schubert (1983) Magnetism and Thermal Evolution of the Terrestrial
1115 Planets, *Icarus, 54*, 466-489.

1116 Yin, A. (2012) Structural analysis of the Valles Marineris fault zone: Possible evidence for large-scale
1117 strike-slip faulting on Mars. *Lithosphere* **4**: 286-330 (doi:10.1130/L192.1).

1118

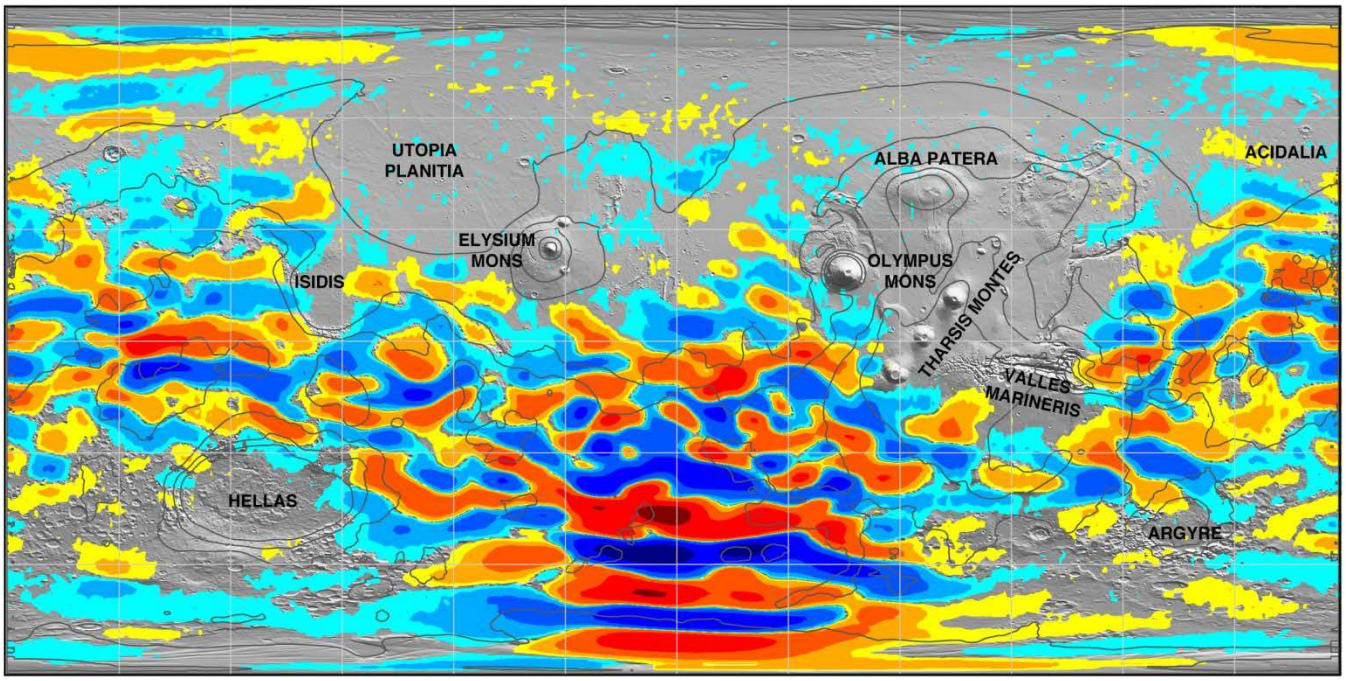

Figure 1: Map of the magnetic field of Mars observed by the Mars Global Surveyor satellite at a nominal 400 km altitude (after *Connerney et al.,* 2005). Each pixel is colored according to the median value of the filtered radial magnetic field component observed within the 1° by 1° degree latitude/longitude range represented by the pixel. Colors are assigned in 12 steps spanning two orders of magnitude variation. Where the field falls below the minimum contour a shaded MOLA topography relief map provides context. Contours of constant elevation (-4, -2, 0, 2, 4 km elevation) are superimposed.

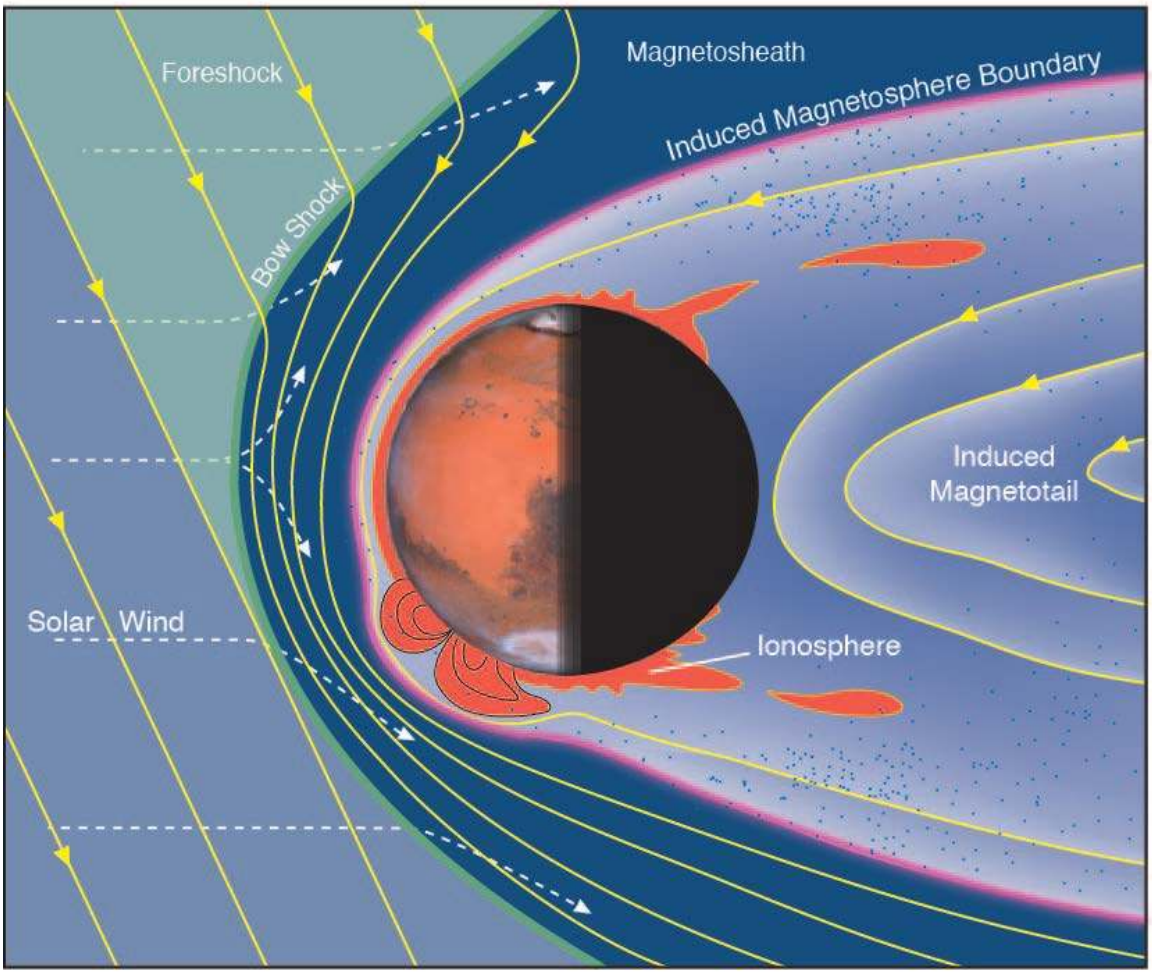

Figure 2: Schematic of the solar wind interaction with Mars (from *Brain et al.,* 2014). The solar wind carries with it the interplanetary magnetic field (yellow) as it streams (dashed lines) toward the bow shock (green) upstream of Mars. Intense crustal magnetic fields (orange) impose structure throughout localized regions of the upper atmosphere and ionosphere.

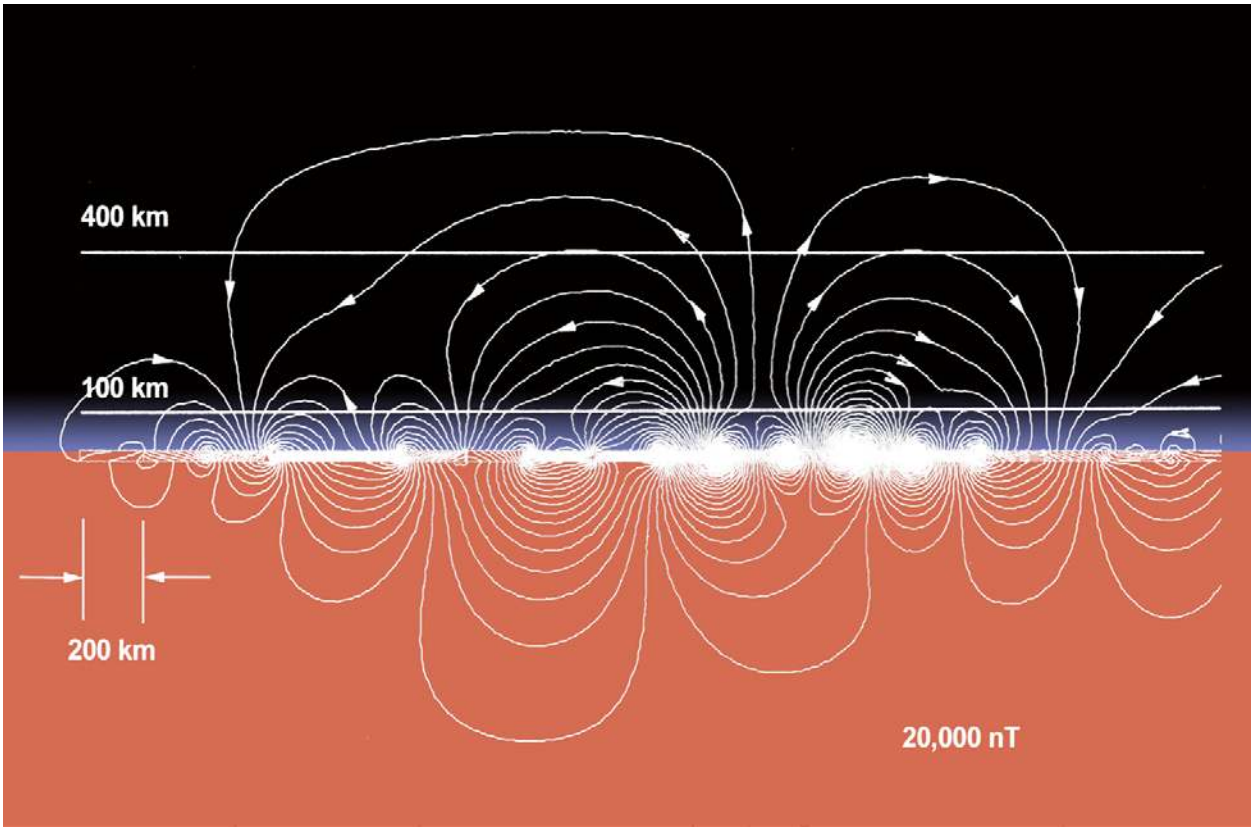

Figure 3: Plane projection of the magnetic field geometry above the intensely magnetized southern highlands based on the crustal magnetic field model of *Connerney et al.,* [1999]. This figure illustrates the field geometry that would be encountered during periapsis passes along a line of constant longitude (near 150 degrees east) and centered at 50 degrees south latitude. Similar "mini-magnetospheres" may be encountered above much of the magnetized crust, depending on spacecraft altitude and solar wind conditions.

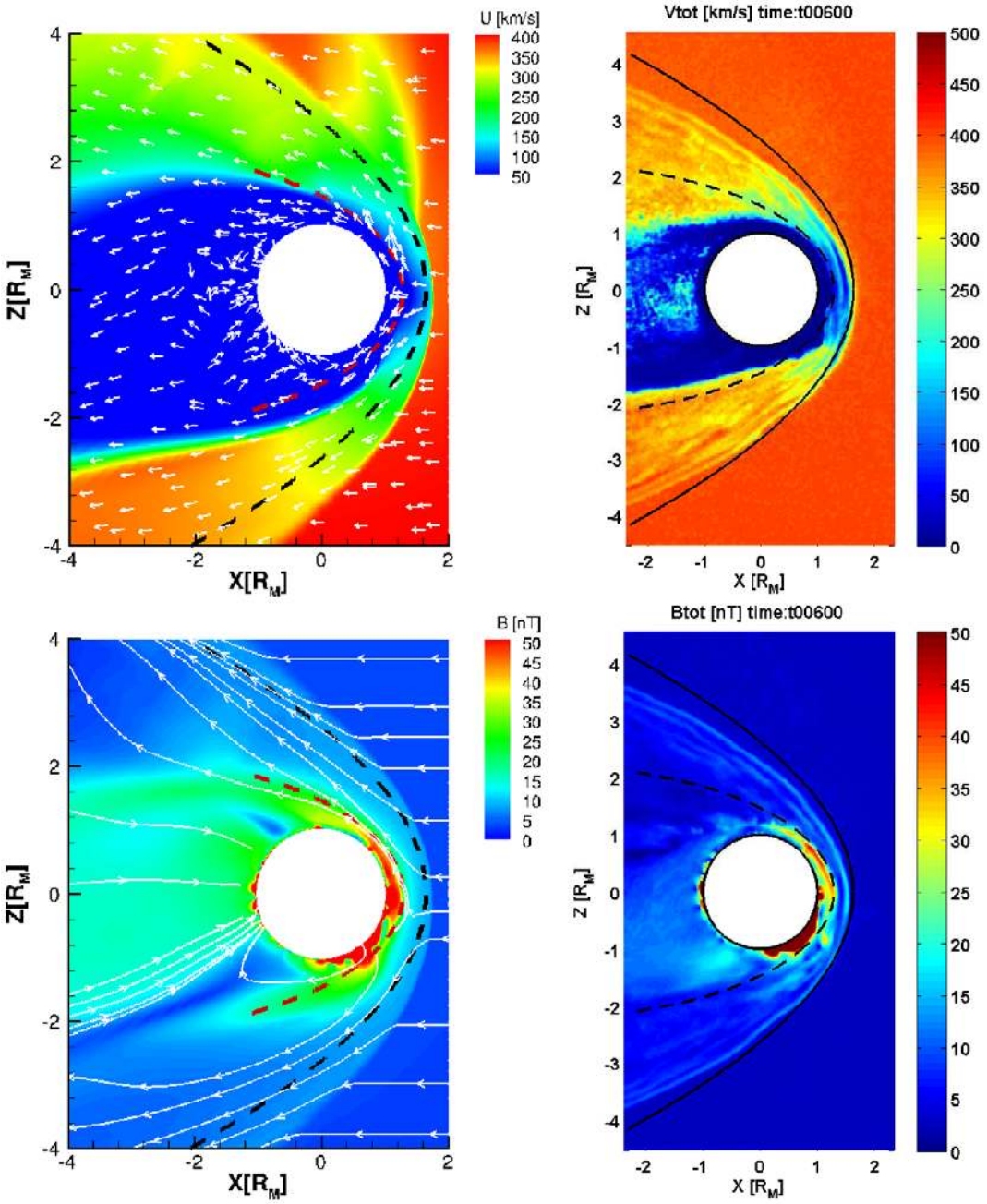

Figure 4: Plasma and magnetic field environment of Mars according to the multi-fluid magnetohydrodynamic simulation of Dong and colleagues [*Dong et al.*, 2014]. Upper left panel is a meridian plane projection of the magnitude (color) and direction (arrows) of plasma velocity near Mars. Lower left panel shows the simulated magnetic field lines and magnetic field magnitude (colors) in meridian plane projection. Large field magnitudes very near the planet's surface are due to strong crustal magnetic fields, primarily in the southern hemisphere, but strong fields due to the solar wind interaction are also encountered at altitude on the day side of the planet.

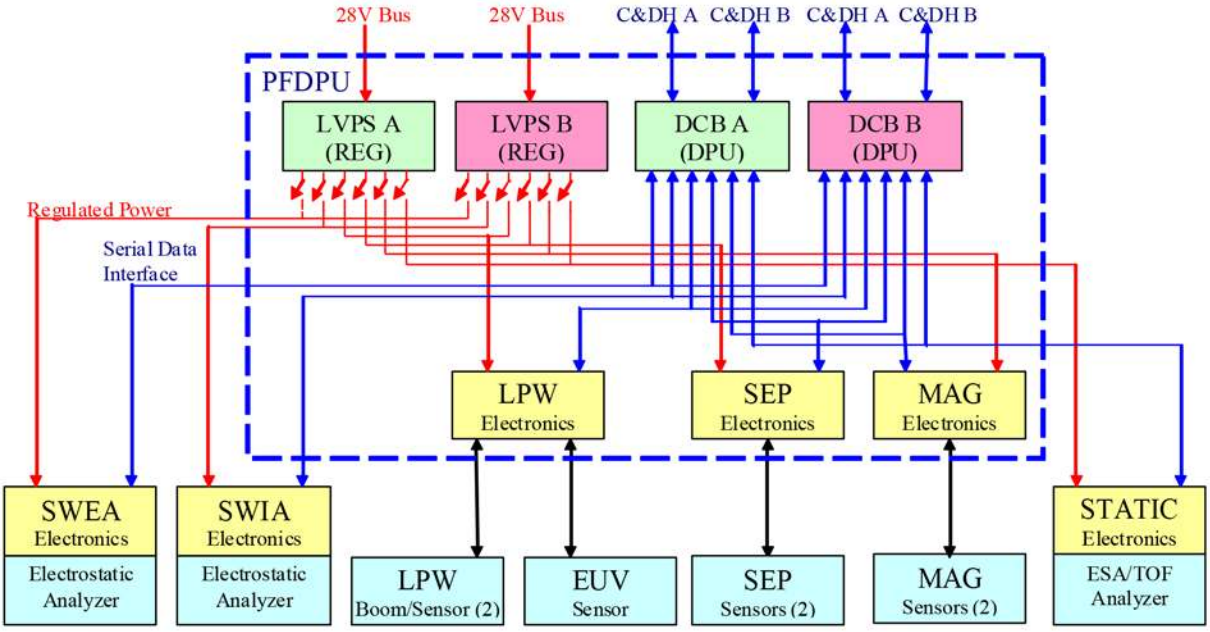

Figure 5: Schematic diagram of the Particles and Fields Package (PFP) and science instrumentation that it services. The PFP Digital Processor Unit (PFPDPU) consolidates instrument power service, command, and telemetry functions for the suite of instruments, presenting a single electrical interface to the spacecraft.

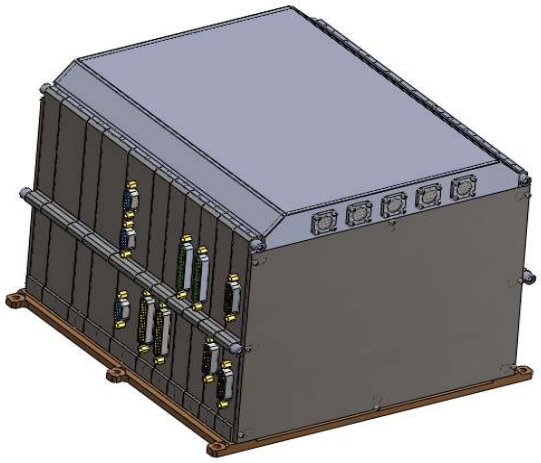

Figure 6: The Particles and Fields electronics stack, accommodates electronics frames for each of the instruments in the suite, in addition to redundant power supplies and command and data handling digital processor units.

Figure 7: The MAVEN spacecraft in the clean room at Lockheed Martin during assembly. The (-Y) MAG sensor (left extremity) is mounted at the end of the MAG "boomlet". A cautionary piece of yellow tape hangs below the sensor. The sensor cover bears laminations of copper tape and Kapton tape providing electrostatic and electromagnetic shielding.

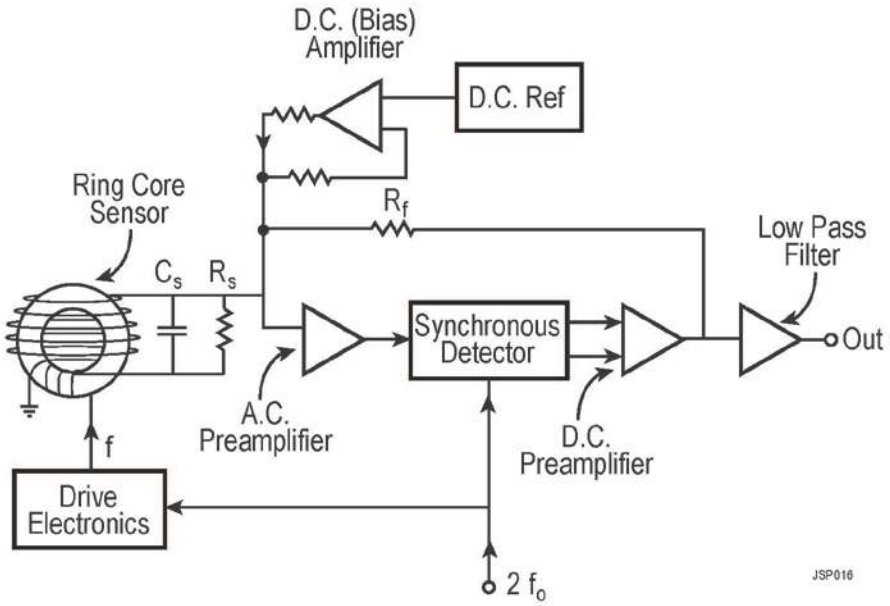

Figure 8: Schematic of a single-axis fluxgate magnetometer (after Acuña, 2002) utilizing a tuned ring-core sensor and a shared 2f sense and feedback coil.

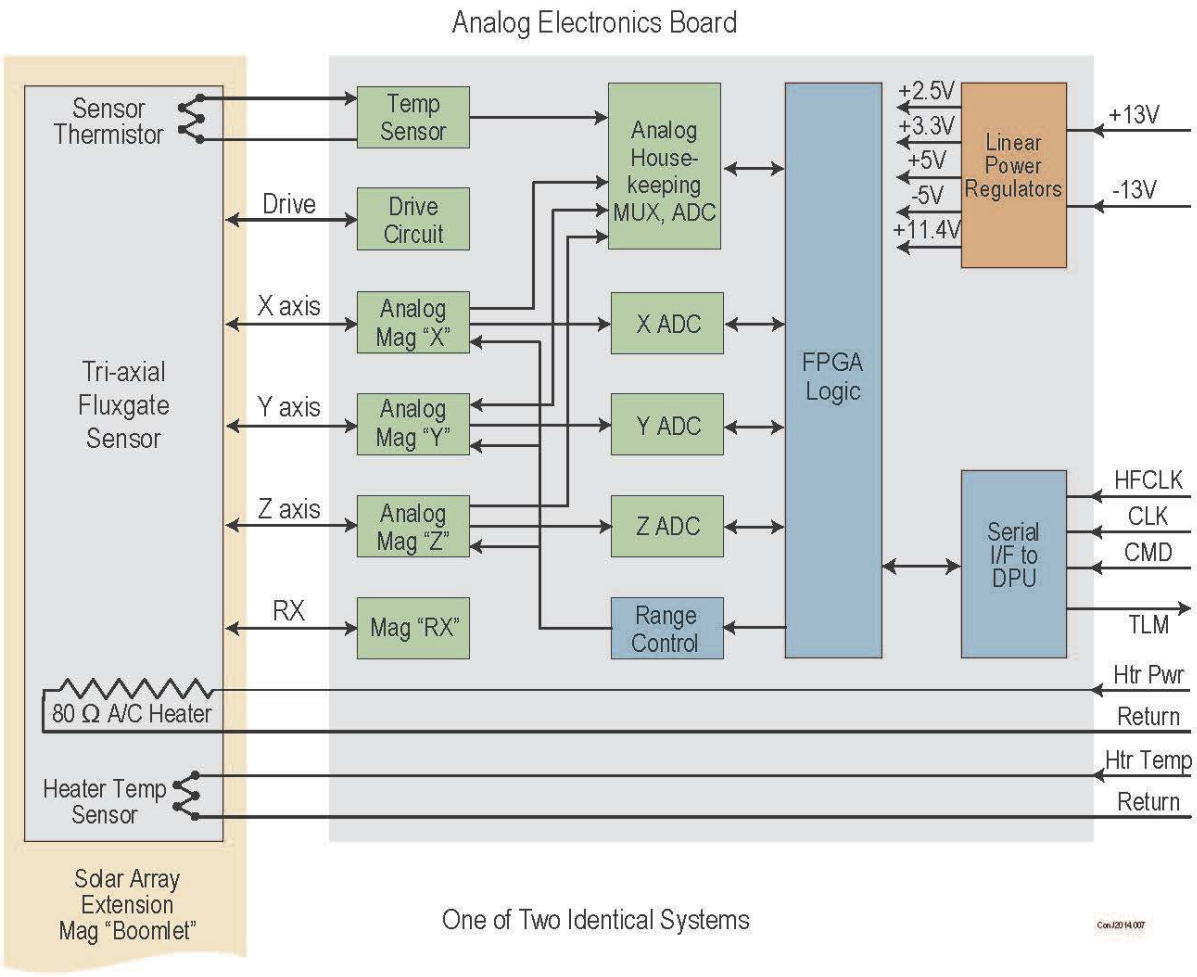

Figure 9: Simplified block diagram of one of the two identical MAVEN vector magnetometers. The tri-axial fluxgate sensor (left) is mounted on the MAG "boomlet" at the end of the solar array and harnessed to the electronics package mounted in the spacecraft body. The analog and digital electronics (right shaded portion) is contained on a single multilayer electronics board that is contained in a shielded enclosure (frame) within the PFP assembly.

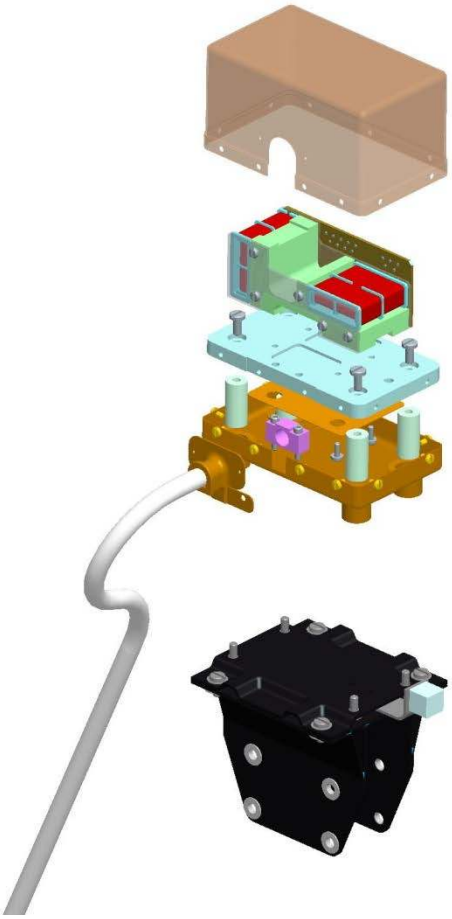

Figure 10: Expanded illustration of the sensor assembly showing the type LE phenolic sensor block (green), nested sense and feedback coils (red), base (blue), thermal isolation feet (light blue), clam-shell protective cover (tan), and carbon composite mounting bracket assembly (black) with attached calibration cube.

Figure 11: Photograph of the MAVEN magnetometer sensor assembly showing the phenolic sensor block (brown), nested sense and feedback coils, and sensor printed circuit board. The sensor is provided with a (shielded) pigtail connector to insure that interconnect hardware is kept at a sensible distance from the sensor; nevertheless, all components installed on the MAG boomlets are subject to enhanced magnetic screening prior to use.

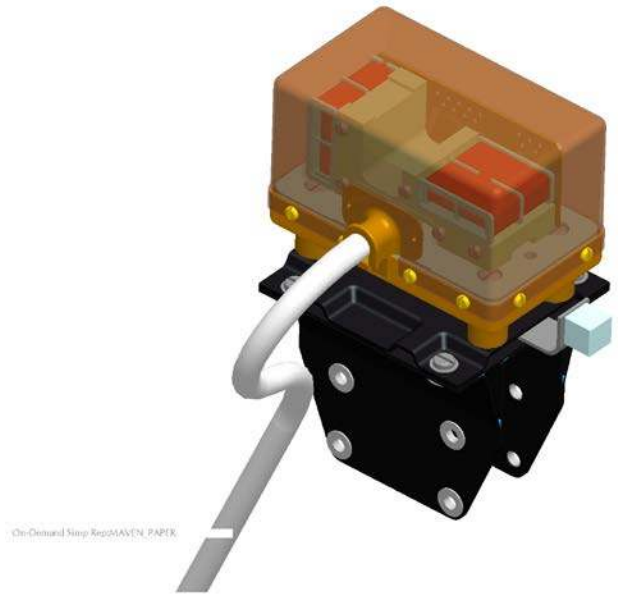

Figure 12: Assembled sensor assembly. Once assembled, all parts of the sensor assembly remain assembled except for the lower part of the carbon composite mounting bracket assembly (black) that attaches to the MAG "boomlet". The top part of the mounting bracket with the attached optical cube remains in assembly with the sensor block throughout the entire test and calibration program.

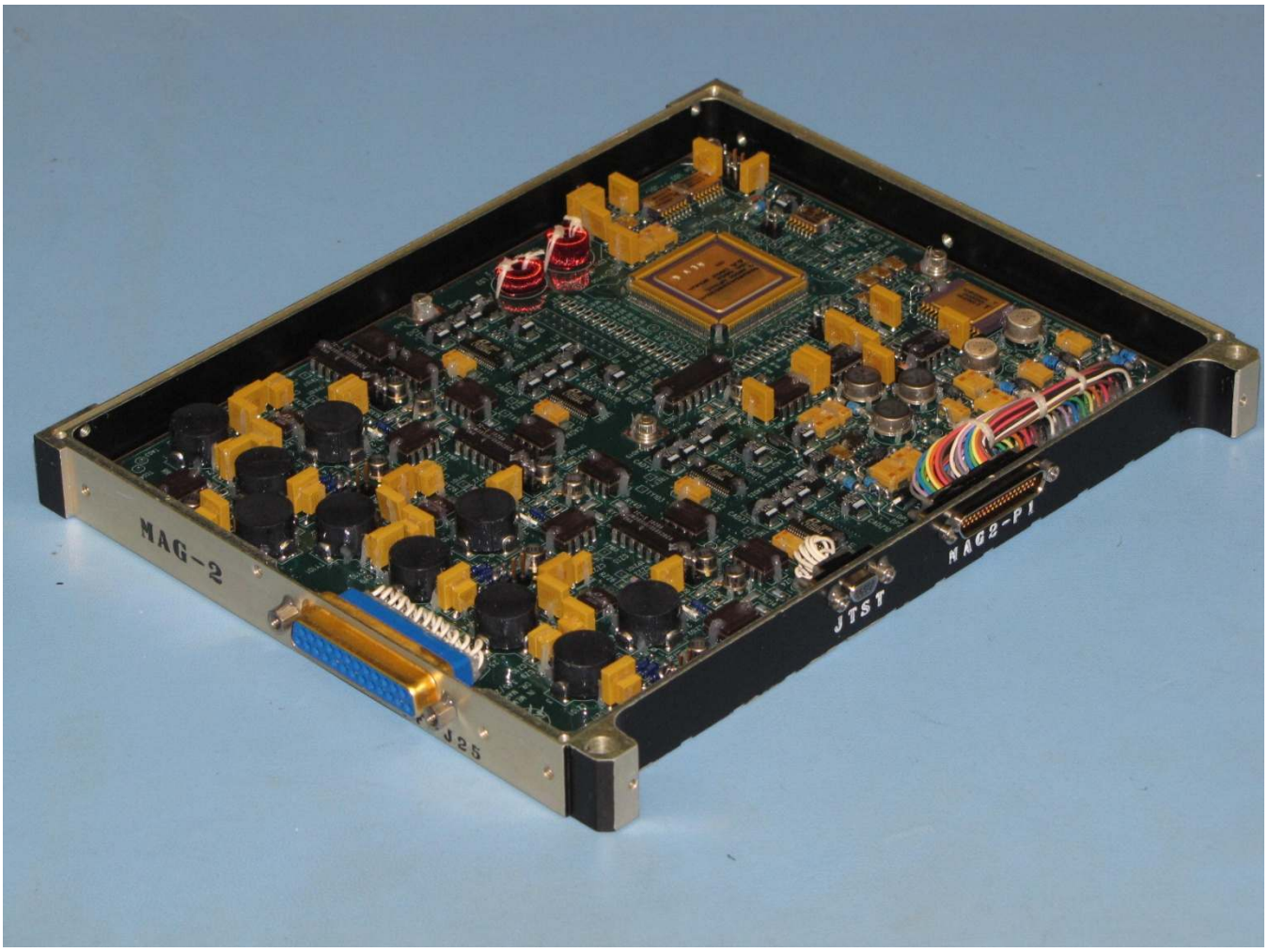

Figure 13: Magnetometer analog and digital board (one of two identical assemblies) in its shielded frame, top cover removed for viewing. The analog portion is to the left, where the sensor cable connector J25 resides, and the digital portion is to the right. The FPGA is the large square device on the upper right.

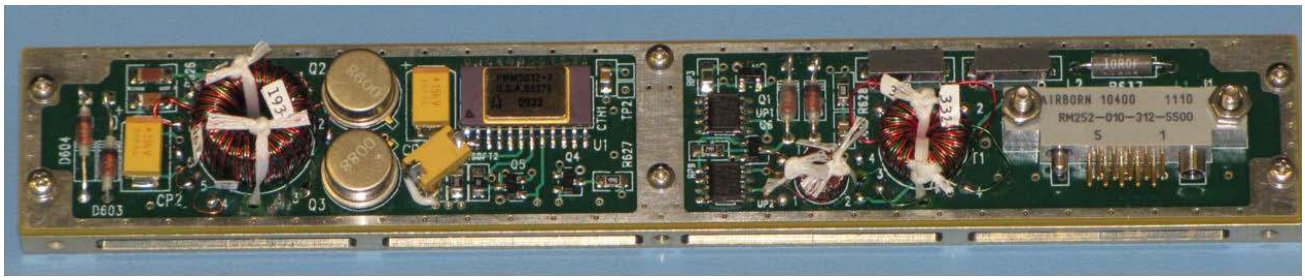

Figure 14: Magnetometer a/c heater board (one of two identical assemblies, mounted back-to-back) in its carrier frame. This assembly is mounted on the PFP instrument interface board.

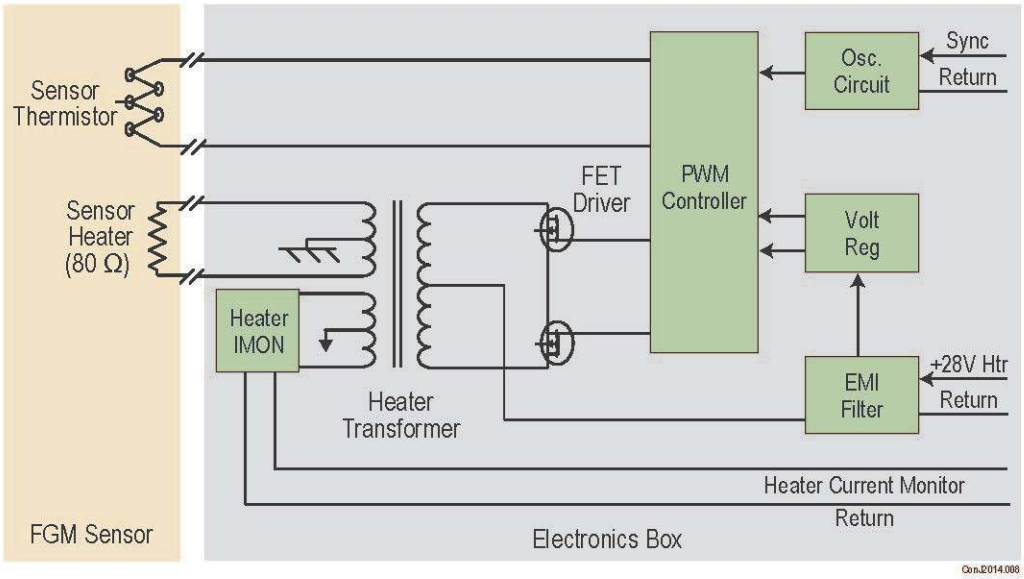

Figure 15: Simplified block diagram of one of the two identical MAVEN a/c heater electronics assemblies. The tri-axial fluxgate sensor (left) is mounted on the MAG "boomlet" at the end of the solar array. The heater control electronics (right shaded portion) is contained on a single multilayer electronics board that is integrated with the PFP instrument interface board (in order to minimize potential interference with sensitive analog electronics). A transformer-coupled heater monitor is made available to the spacecraft engineering telemetry so that the thermal power delivered to the MAG sensors may be monitored when the MAG electronics is powered off.

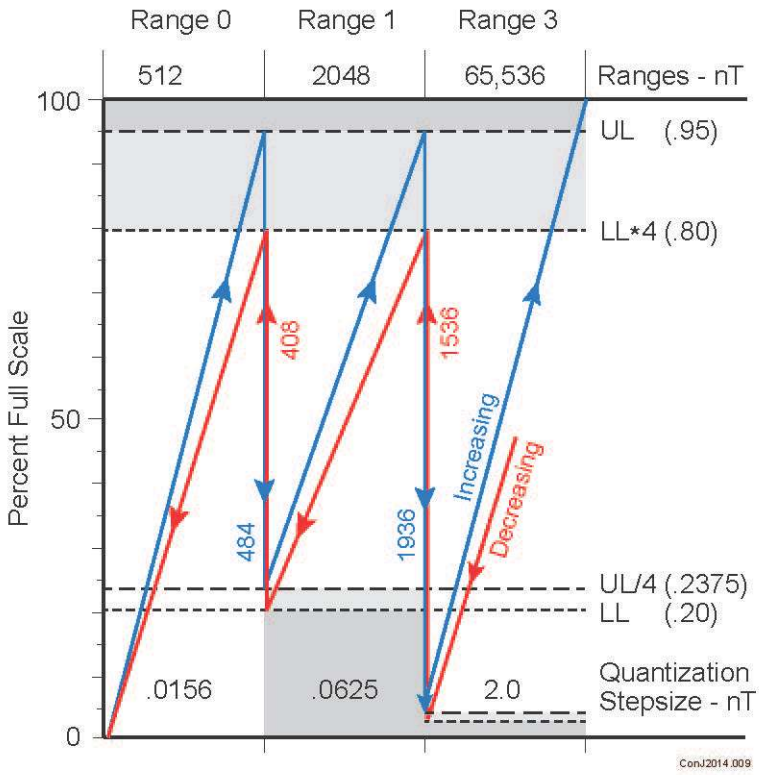

Figure 16: Instrument autonomous range selection algorithm increases the instrument dynamic range to prevent saturation in response to an increasing (blue) magnetic field magnitude in any of the three vector components and decreases instrument dynamic range in response to a decreasing field (red). The algorithm uses "guard bands" to prevent rapid back and forth changes in dynamic range ("toggling") in the presence of field fluctuations near range limits. Nominal threshold values are shown.

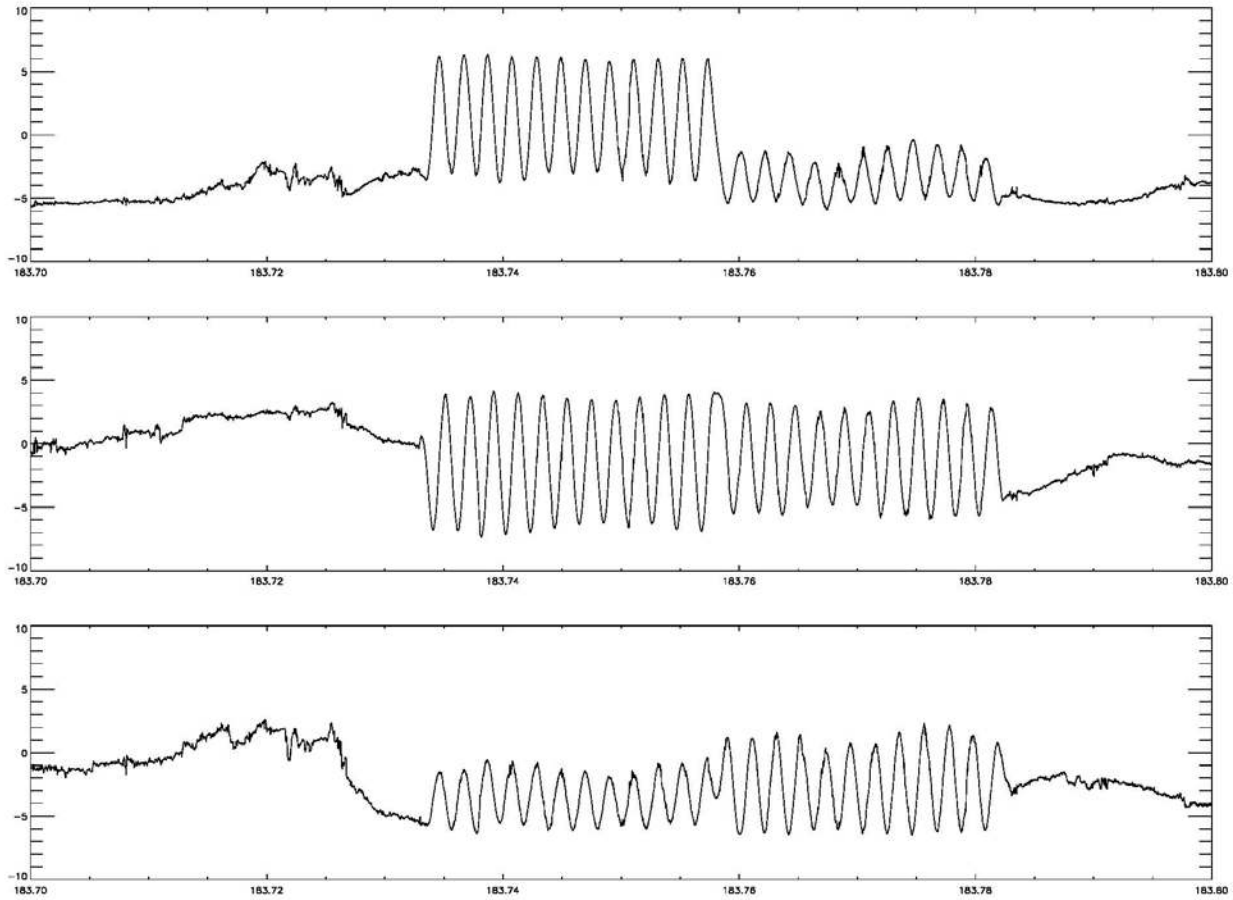

Figure 17: Magnetic field in spacecraft payload coordinates throughout the second cruise MAGROLL maneuver on DOY 183, 2014, during which the spacecraft executes a rolls at 2 degrees/s about a principal axis (near the z axis), followed by rolls about an orthogonal axis (near spacecraft x). Instrument dynamic range was commanded to manual range 1 (+/- 2048 nT) for the first few rolls about z, followed by rolls about both z and x in range 0 (+/- 512 nT), followed by rolls about x in range 1. After completion of the sequence, the instruments are returned to autorange mode.

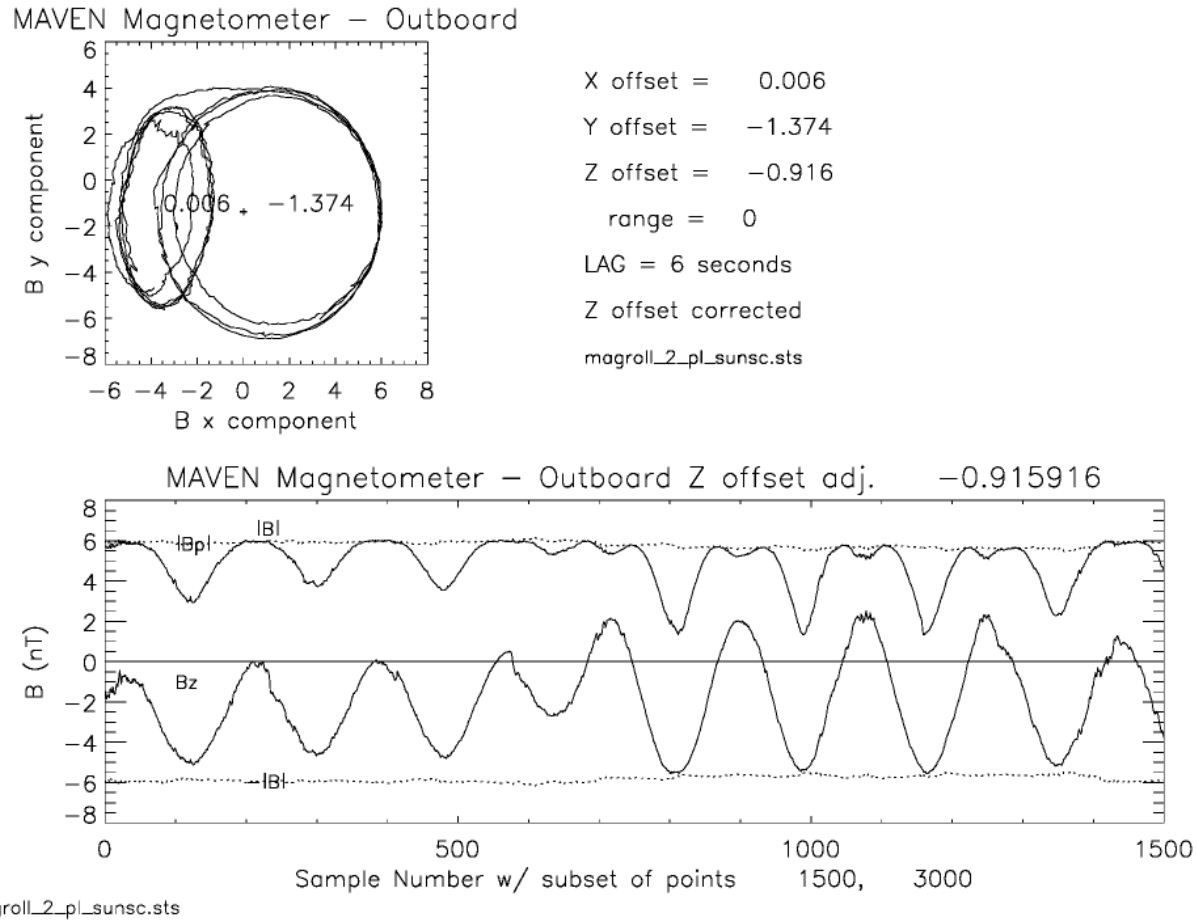

Figure 18: Application of offset estimation to range 0 (+/- 512 nT range) observations obtained during the second cruise magroll exercise, using a six second lag for vector differences, during which the field rotates in the sc reference frame by 12 degrees. The figure in the upper left is a diagnostic hodogram of B_y vs B_x. In the lower figure a time series of the field magnitude and the negative of the field magnitude is shown (dotted line) demonstrating little spin modulation with the estimated offsets applied to the vector observations.

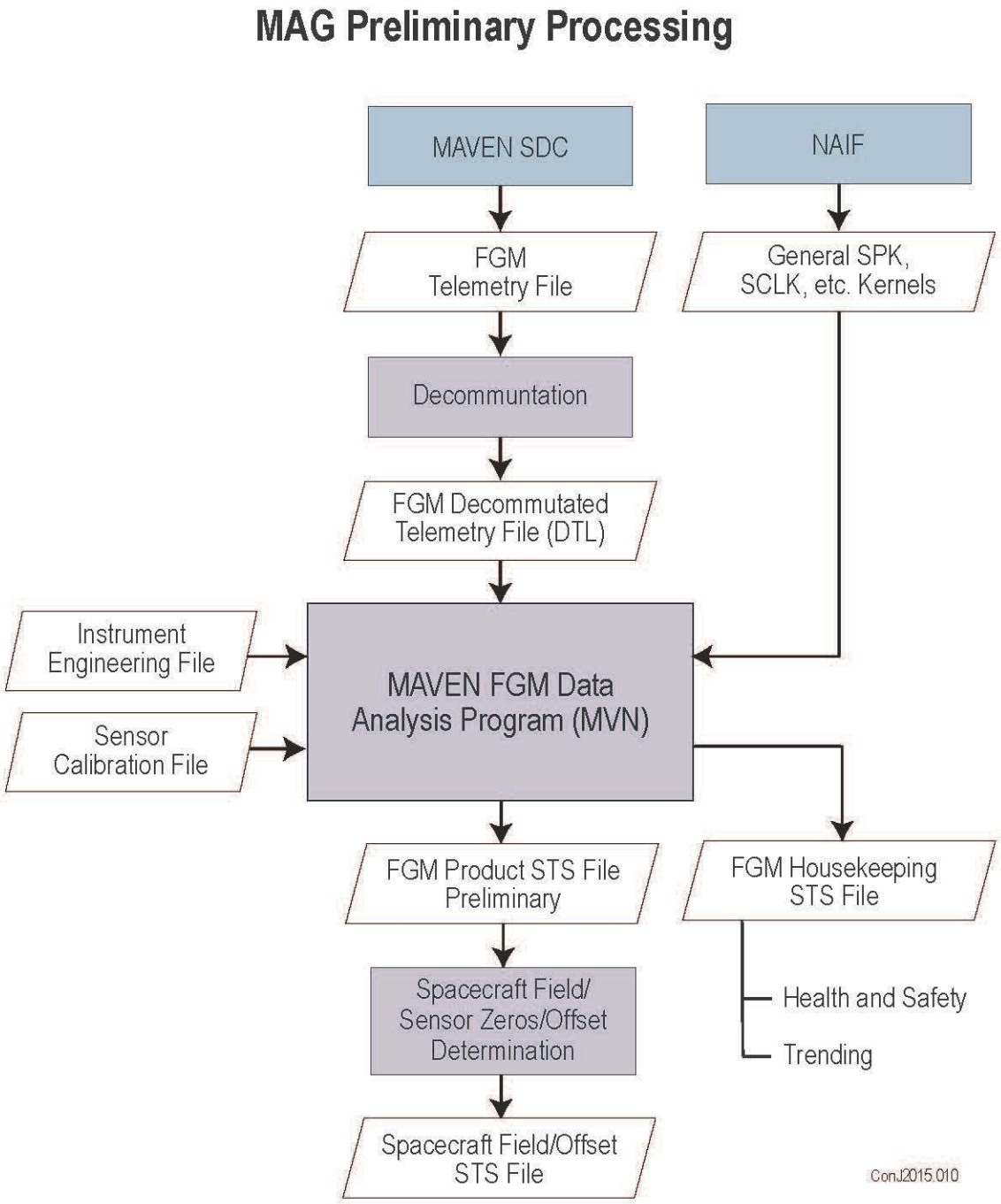

Figure 19: Flow diagram of the preliminary MAG data processing. Preliminary processing is done prior to receipt of supplementary spacecraft engineering data (e.g., solar array currents), reconstructed spacecraft ephemeris, and attitude kernels, to assess instrument health and safety and to estimate sensor zeros and/or static spacecraft magnetic fields.

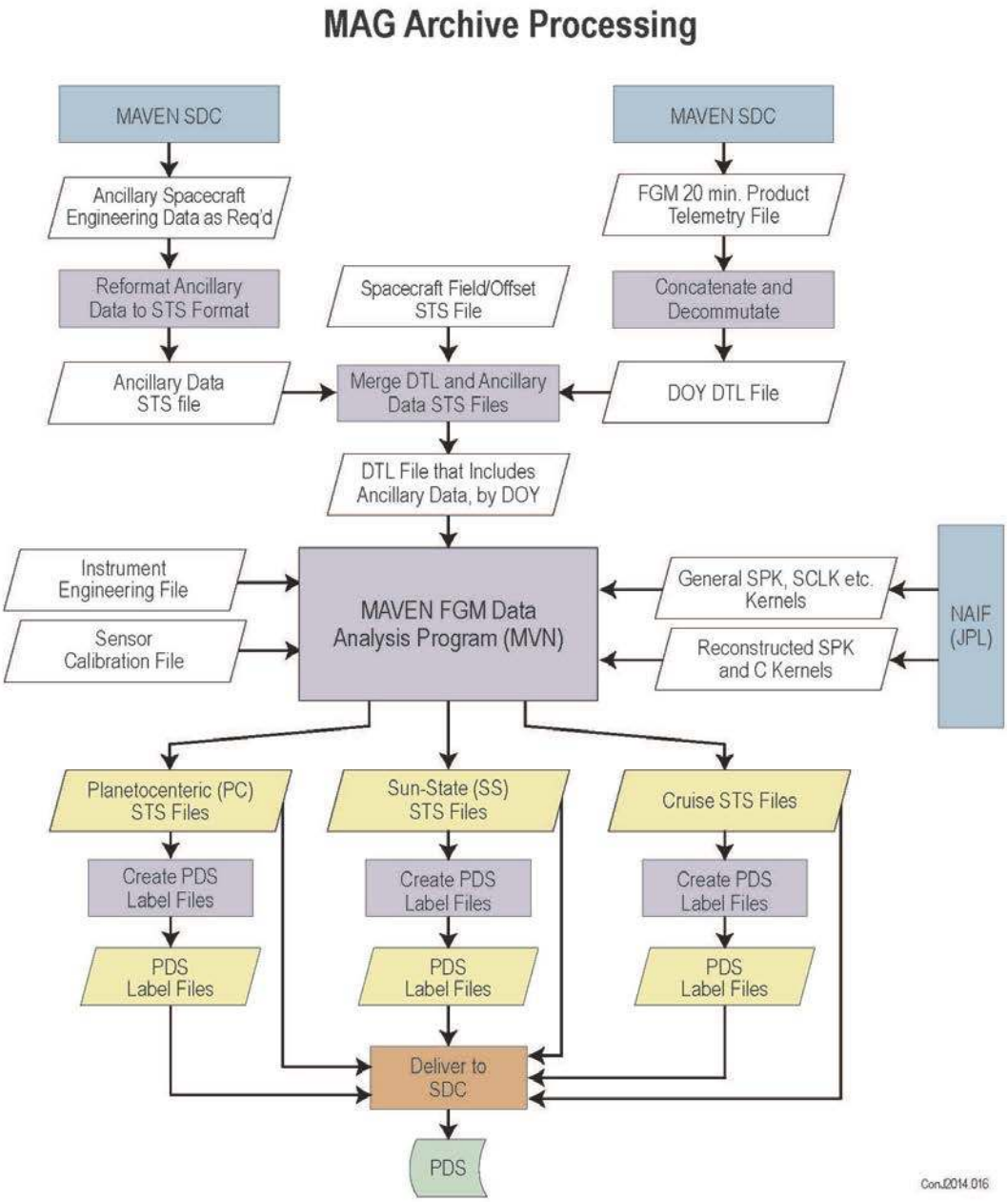

Figure 20: Flow diagram of MAG final data processing. Final processing is done subsequent to receipt of reconstructed spacecraft ephemeris and attitude kernels using the same program elements. Data files containing time-ordered records of fully-calibrated magnetic field vectors, rendered in several useful coordinate systems, are the archive data products. Each record contains spacecraft position rendered in the appropriate coordinate system along with supplementary engineering data, where useful.